

# Spectroastrometry and Reverberation Mapping: the Mass and Geometric Distance of the Supermassive Black Hole in the Quasar 3C 273

YAN-RONG LI <sup>1</sup>, JIAN-MIN WANG <sup>1,2,3</sup>, YU-YANG SONGSHENG <sup>1</sup>, ZHI-XIANG ZHANG,<sup>4</sup> PU DU <sup>1</sup>, CHEN HU,<sup>1</sup> AND MING XIAO<sup>1</sup>

<sup>1</sup>Key Laboratory for Particle Astrophysics, Institute of High Energy Physics, Chinese Academy of Sciences, 19B Yuquan Road, Beijing 100049, China

<sup>2</sup>National Astronomical Observatories of China, Chinese Academy of Sciences, 20A Datun Road, Beijing 100012, China

<sup>3</sup>School of Astronomy and Space Science, University of Chinese Academy of Sciences, 19A Yuquan Road, Beijing 100049, China

<sup>4</sup>Department of Astronomy, Xiamen University, Xiamen, Fujian 361005, China

(Received 2021 August 7; Revised 2021 October 27; Accepted 2022 January 10)

Submitted to *The Astrophysical Journal*

## ABSTRACT

The quasar 3C 273 has been observed with infrared spectroastrometry (SA) on broad Pa $\alpha$  line and optical reverberation mapping (RM) on broad H $\beta$  line. SA delivers information about the angular size and structure of the Pa $\alpha$  broad-line region (BLR), while RM delivers information about the physical size and structure of the H $\beta$  BLR. Based on the fact that the two BLRs share the mass of the supermassive black hole (SMBH) and viewing inclination, a combination of SA and velocity-resolved RM (SARM) thereby allows us to simultaneously determine the SMBH mass and geometric distance through dynamically modeling the two BLRs. We construct a suite of dynamical models with different geometric configurations and apply a Bayesian approach to obtain the parameter inferences. Overall the obtained masses and distances are insensitive to specific BLR configurations but more or less depend on parameterizations of the vertical distributions. The most probable model, chosen in light of the Bayes factor, yields an angular-size distance of  $\log(D_A/\text{Mpc}) = 2.83_{-0.28}^{+0.32}$  and SMBH mass of  $\log(M_\bullet/M_\odot) = 9.06_{-0.27}^{+0.21}$ , which agrees with the relationships between SMBH masses and bulge properties. The BLRs have an inclination of  $5_{-1}^{+1}$  degrees, consistent with that of the large-scale jet in 3C 273. Our approach reinforces the capability of SARM analysis to measure SMBH mass and distance of AGNs even though SA and RM observations are undertaken with different emission lines and/or in different periods.

**Keywords:** Active galaxies (17); Quasars (1319); Supermassive black holes (1663); Reverberation mapping (2019); Astrometry (80)

## 1. INTRODUCTION

Active galactic nuclei (AGNs) and quasars are those the brightest objects at cosmic distances that are believed to be powered by matter feeding into supermassive black holes (SMBHs) residing at their centers. One of hallmark properties of their electromagnetic radiations is the presence of prominent broad emission lines with typical widths of several thousands kilometers per second (e.g., Netzer 2013). It is long known that the regions responsible for broad emission lines, the so called broad-line regions (BLRs), must be compact and located well within the centers of AGNs and quasars as as to produce sufficiently large Doppler shifting velocities and explain the observed line widths (e.g., Woltjer 1959; Burbidge et al. 1963; Rees 1977). These broad emission lines have been of central importance to unveil gaseous

environments and dynamics in the vicinity of SMBHs. However, because of limited spatial resolution of observations, it had always been challenging to determine fine structures and dynamics of BLRs in AGNs and quasars.

The reverberation mapping (RM) technique, originating from the pioneering works of Bahcall et al. (1972) and Blandford & McKee (1982), swaps spatial resolution for time resolution by measuring temporal responses of variations of broad emission lines to those of the driving continuum emitted by the accretion disk (Peterson 1993). These responses show time delays due to the light-travel time from the accretion disk to the BLR and thus encode information about BLR structure and kinematics perpendicular to the iso-delay surfaces. Starting in the late 1980s, RM observation campaigns have significantly advanced our understanding of BLRs and most importantly, have led to the establishment of RM as a promising method for measuring SMBH masses in AGNs (e.g., Kaspi et al. 2000; Bentz et al. 2013; Du & Wang 2019; see also a review in Peterson 2014).

On the other hand, after decades of persistent endeavors, the GRAVITY instrument onboard the Very Large Telescope Interferometer (VLTI; Gravity Collaboration et al. 2017) successfully resolved, for the first time, the Pa $\alpha$  BLR in the quasar 3C 273 with an angular resolution down to  $\sim 10$  micro arcseconds (Gravity Collaboration et al. 2018, hereafter G18). This achievement marked a giant step towards the era of high angular resolution astronomy in the field of AGNs and most importantly, ushered in the practical feasibility of applying the spectroastrometry (SA) technique to understand BLR physics (Beckers 1982; Bailey 1998). The GRAVITY/VLTI instrument measures SA signals of the BLR, namely, astrometry along with wavelength (or velocity), through interferometric phases. Because different parts of the BLR have different Doppler shifting velocities and photocenters (or angular displacements), SA can therefore resolve angular structures of the BLR perpendicular to the line of sight (LOS; e.g., Rakshit et al. 2015; Gravity Collaboration et al. 2020a). Besides through interferometry, SA can also be applied through spectroscopy with the forthcoming next-generation single-aperture telescopes, such as the Extremely Large Telescope, the Thirty Meter Telescope, and the Giant Magellan Telescope, all which are expected to attain an angular resolution of several tens of micro arcseconds (e.g., Stern et al. 2015; Bosco et al. 2021).

With the successful SA observation of G18, Wang et al. (2020, hereafter W20) made the first effort to integrate the SA technique (in spatial domain) with the reverberation mapping (RM) technique (in time domain) and conducted the joint SA and RM (hereafter SARM) analysis on the data of 3C 273 (G18; Zhang et al. 2019). A second case of SARM analysis was recently conducted by Gravity Collaboration et al. (2021a) upon the nearby galaxy NGC 3783. The capability of such SARM analysis is twofold. First, SA and RM are complementary in the sense that they probe different dimensions of BLR structures. SARM analysis thus leverages this property and offers new physical information about BLRs (compared to sole SA or RM analysis). Second, the linear BLR structures from RM together with angular BLR structures from SA naturally constitute a basic probe to geometric distances of AGNs and quasars. In this regard, the SARM approach paves an elegant pathway for the long-term epic pursuits of using AGNs and quasars for cosmology, which date back to 1960s soon after the discovery of the first quasar 3C 273 (e.g., Sandage 1965; Hoyle & Burbidge 1966; Longair & Scheuer 1967; Schmidt 1968; Bahcall & Hills 1973; Baldwin 1977; Elvis & Karovska 2002; Watson et al. 2011; Wang et al. 2013; Hönicg et al. 2014; La Franca et al. 2014; Risaliti & Lusso 2019; Gravity Collaboration et al. 2021).

For 3C 273, SA observed the infrared Pa $\alpha$  line (G18) whereas RM observed the optical H $\beta$  line (Zhang et al. 2019). It is known that profiles of H $\beta$  and Pa $\alpha$  lines in AGNs are generally not consistent in light of both widths and shapes (Landt et al. 2008; Kim et al. 2010; Durré & Mould 2021). Specifically, Kim et al. (2010) reported that the full widths at half maximum (FWHMs) of H $\beta$  lines are systematically broader than those of Pa $\alpha$  lines by about  $\sim 30\%$ . This clearly

implies that the respective BLRs of the two lines are different in some aspects (e.g., optical depths). Because only using 1D RM<sup>1</sup> data, the SARM analysis in W20 needed to presume a common BLR for the two lines and neglected their possible differences. It is therefore highly worth extending the work of W20 by developing a more generic framework. As we show below, through combining SA data and 2D (or velocity-resolved) RM data in a way that the corresponding BLRs only share some physical parameters (such as black hole mass and inclination), 2D SARM analysis can resolve not only the problem of different emission lines in the two data sets, but also the issue that SA measures emissivity-weighted photocenters of the BLR, whereas RM measures responsivity-weighted parts of the BLR (e.g., Goad et al. 1993). Besides, such a new approach of SARM analysis does not even require SA and RM data to be observed in the same periods, therefore greatly strengthening the applicability of SARM analysis.

The paper is organized as follows. Section 2 compiles SA and RM data as well as compares the profiles of the extracted H $\beta$  and Pa $\alpha$  lines. Section 3 introduces BLR dynamical modeling on SA and RM data and constructs a suite of BLR models. In Section 4, we detail the procedure for joint SA and 2D RM analysis. In Section 5, we summarize the main results of our joint analysis. Discussions and conclusions are given in Sections 6 and 7, respectively.

Throughout the paper, we use the redshift  $z = 0.15834$  of 3C 273 retrieved from the NASA/Infrared Process and Analysis center (IPAC) Extragalactic Database, with which we convert the wavelength to the rest frame and correct for the cosmological time dilation. The Galactic extinction along the direction of 3C 273 is corrected using a color excess of  $E(B - V) = 0.018$  and the Fitzpatrick (1999) parameterization.

## 2. DATA

### 2.1. Spectroastrometric Data

The SA data of 3C 273 were reported by G18, which made observations using the GRAVITY/VLTI (Gravity Collaboration et al. 2017) on eight nights between July 2017 and May 2018. The instrument measures the interferometric visibility amplitudes and phases on each of six baselines (telescope pairs) by coherently combining the light from the four 8m telescopes. Gravity Collaboration et al. (2020b) reported the measured visibility amplitudes for 3C 273, which are dominated by the visibilities of the continuum emission from hot dusts. G18 averaged the exposures of adjacent epochs to reduce measurement noises and published the differential phase curves (relative to a reference continuum wavelength) as a function of wavelength for six baselines on four (averaged) epochs (see extended data Figure 1 therein). To calcu-

<sup>1</sup> Here, 1D RM means that only velocity-integrated fluxes of the broad emission line are used in RM analysis and the velocity dimension is not taken into account. Oppositely, 2D (or velocity-resolved) RM means that the additional velocity dimension is included.

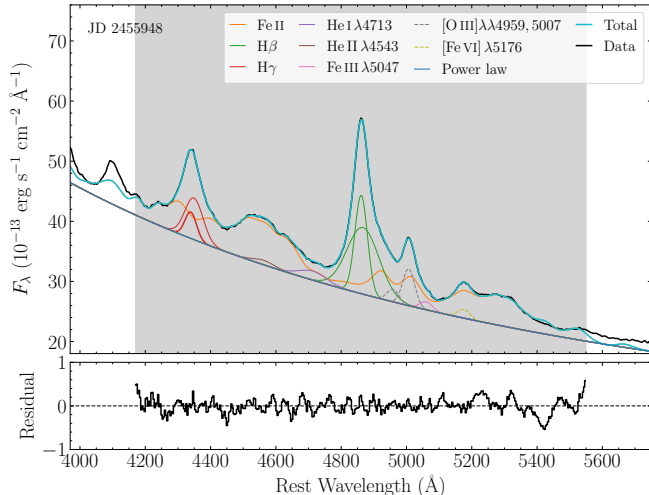


**Figure 1.** An example for a multi-component decomposition of the spectrum at JD 2455948. Grey shaded area represents the wavelength window for the spectral decomposition.

late differential phases with a BLR dynamical model, the  $\text{Pa}\alpha$  profile normalized by the underlying continuum flux is also needed. We use the mean  $\text{Pa}\alpha$  profile over the eight epochs between July 2017 and May 2018 published by G18. We use a Gaussian to model the GRAVITY spectral broadening with a standard deviation of  $235 \text{ km s}^{-1}$  (G18).

## 2.2. Reverberation Mapping Data

The RM campaign of 3C 273 was reported by Zhang et al. (2019), which synthesized the spectroscopic and photometric data from the Steward Observatory spectropolarimetric monitoring project<sup>2</sup> (Smith et al. 2009) and the super-Eddington accreting massive black hole project (Du et al. 2014). These two projects employed different kinds of spectrographs and the yielded data differed in spectral resolutions and flux calibrations. The majority of the spectroscopic data come from the Steward Observatory, therefore, for the sake of data homogeneity, we only use the Steward Observatory’s data. There were in total 386 spectra during the period between November 2008 and July 2018, out of which 301 spectra were calibrated to match the  $V$ -band magnitude taken on the same night and the rest 75 spectra could not be calibrated as such because of lacking contemporaneous photometry. We further discard 23 spectra taken under an airmass  $\geq 2.0$ . In addition, there were double exposures in eight epochs of the remaining spectra. We combine those double exposures on the same night into one and finally get 270 spectra.

To extract the broad  $\text{H}\beta$  emission line from the spectra, we implement a spectral decomposition scheme described in Hu et al. (2012) and Barth et al. (2013), using the `DASpec` software<sup>3</sup>, which determines all spectral components simultane-

ously by minimizing the  $\chi^2$  via the Levenberg–Marquardt technique. The spectral fitting window is set to be 4170–5550 Å (in rest frame). We include the following spectral components: 1) a single power law for the featureless continuum; 2) a Fe II template from Boroson & Green (1992) to represent the optical blended Fe II emissions; 3) single Gaussians for the  $[\text{O III}]\lambda\lambda 4959, 5007$ . The fluxes of  $[\text{O III}]\lambda 4959$  is fixed to be one-third of those of  $[\text{O III}]\lambda 5007$  (e.g., Peterson et al. 2004); 4) double Gaussians for the broad  $\text{H}\beta$  and  $\text{H}\gamma$  lines; 5) a single Gaussian for the broad He I  $\lambda 4713$  line (e.g., Véron et al. 2002). This line is strongly blended with the blue wing of the  $\text{H}\beta$ . To reduce the degeneracy, we fix a zero velocity shift for this line component. The narrow-line components for the  $\text{H}\beta$  and  $\text{H}\gamma$  lines are not included because the  $[\text{O III}]$  lines are quite weak, indicating that the narrow  $\text{H}\beta$  component is negligible.

Besides the above components, there are additional significant components around 4543 Å, 5047 Å, and 5176 Å, which might either correspond to He II, Fe III, and  $[\text{Fe VI}]$  emissions, respectively, or be ascribed to the Fe II emissions that are not accounted in the template. We use single Gaussians to represent these components. In particular, the profile width and velocity offset of the  $[\text{Fe VI}]$  line are tied to those of the  $[\text{O III}]\lambda 5007$ . The host starlight component is not included as its contribution to the total flux is estimated to be less than 6% from the host image decomposition (see Zhang et al. 2019 for a detail). We note that compared to the spectral decomposition scheme in Zhang et al. (2019), we additionally include broad  $\text{H}\gamma$ , He I  $\lambda 4713$  line, and Gaussian components around 4543 Å and 5047 Å to further improve the spectral fitting.

After running the above spectral decomposition scheme over all spectra, we obtain the wavelength offset of the  $[\text{O III}]\lambda 5007$  for each spectrum. We find that the mean offset is almost equal to zero, but the dispersion is as large as 2.6 Å. It is therefore necessary to correct for the wavelength offset by aligning the center wavelengths of the  $[\text{O III}]\lambda 5007$ . We finally rerun the above spectral decomposition scheme again and obtain the broad  $\text{H}\beta$  profile by subtracting all the other components from each spectrum. In Figure 1, we show an example for the decomposition of the spectrum at JD 2455948.

We estimate the spectral broadening arising from the instrument and seeing by comparing the  $[\text{O III}]\lambda 5007$  line width to the intrinsic width that can be deduced from other-wise observations with well-determined echelle line spread functions. Following Zhang et al. (2019), we use the spectrum<sup>4</sup> of 3C 273 observed on January 31, 1999 using grating G750L of the Space Telescope Imaging Spectrograph (STIS) onboard the *Hubble Space Telescope* (HST) and apply the above spectral decomposition scheme to determine the observed FWHM of the  $[\text{O III}]\lambda 5007$  line ( $1.97 \pm 0.03$ )  $\times 10^3 \text{ km s}^{-1}$ . By subtracting the STIS’ instrumental resolution of  $439 \text{ km s}^{-1}$  in quadrature, we derive the intrinsic

<sup>2</sup> The website is at <http://james.as.arizona.edu/~psmith/Fermi/>

<sup>3</sup> Available at <https://github.com/PuDu-Astro/DASpec>.

<sup>4</sup> The spectrum is extracted from the dataset O44301020 of the HST archives.

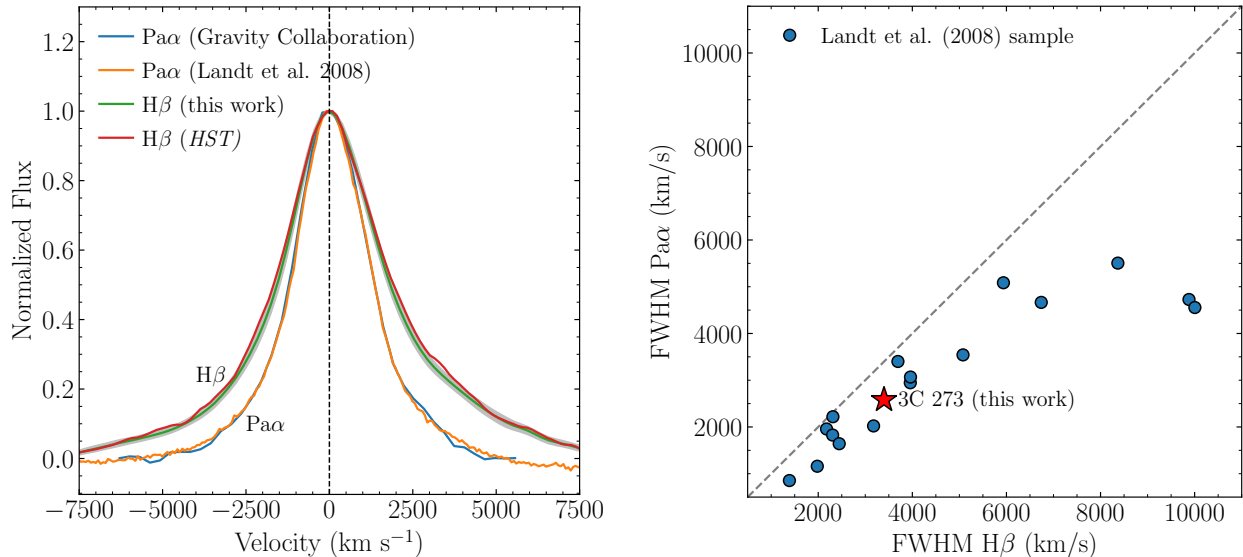


**Figure 2.** (Left) A comparison between the broad  $H\beta$  and  $Pa\alpha$  profiles of 3C 273. Grey shaded area represents the standard deviation of the mean  $H\beta$  profile from the RM observations (see the text for a detail). (Right)  $Pa\alpha$  FWHMs with  $H\beta$  FWHMs for a sample of AGNs compiled by Landt et al. (2008). The location of 3C 273 from this work is highlighted by an asterisk. Note that Landt et al. (2008) used a different scheme for extracting the broad line components, but there is a general consensus that  $H\beta$  lines are systematically broader than  $Pa\alpha$  lines.

[O III] $\lambda$ 5007 line width to be  $(1.92 \pm 0.03) \times 10^3 \text{ km s}^{-1}$ . We then subtract this intrinsic width from the observed [O III] $\lambda$ 5007 line widths of our RM spectra to obtain the spectral broadening at each epoch, which generally ranges from  $\sim 800 \text{ km s}^{-1}$  to  $\sim 1400 \text{ km s}^{-1}$  with a mean of  $1121 \text{ km s}^{-1}$  and standard deviation of  $203 \text{ km s}^{-1}$ .

### 2.3. A Comparison of the Broad $H\beta$ and $Pa\alpha$ Lines

In the left panel of Figure 2, we compare the profiles of the broad  $H\beta$  from the mean spectrum of the RM data and  $Pa\alpha$  lines from the SA data. We also superimpose the broad  $H\beta$  and  $Pa\alpha$  lines extracted from the *HST* spectrum observed on January 31, 1999 (see Section 2.2) and the infrared spectrum of 3C 273 observed by Landt et al. (2008) on June 12, 2006, respectively. Both the normalized  $H\beta$  and  $Pa\alpha$  line profiles do not show noticeable changes between epochs spanning longer than a decade, plausibly implying that the BLRs in 3C 273 are dynamically stable over such a timescale.

The mean  $H\beta$  profile has an FWHM of  $\sim 3200 \text{ km s}^{-1}$  while the  $Pa\alpha$  profile has an FWHM of  $\sim 2500 \text{ km s}^{-1}$ , narrower than the  $H\beta$  profile by a factor of  $\sim 30\%$ . In the right panel of Figure 2, we plot  $Pa\alpha$  and  $H\beta$  line widths for an AGN sample measured by Landt et al. (2008) and superimpose the widths of 3C 273 from this work for sake of comparison. We note that Landt et al. (2008) used a different scheme for extracting the broad line components. Nevertheless, we can find a general consensus that  $H\beta$  lines are systematically broader than  $Pa\alpha$  lines (see also Kim et al. 2010). In addition, the left panel of Figure 2 illustrates that the  $H\beta$  profile is slightly asymmetric, with a minor excess in the red wing. By contrast, the  $Pa\alpha$  profile is relatively symmetric.

The above factors indicate that the geometry and/or kinematics of the  $H\beta$  and  $Pa\alpha$  emission regions might not be the

same. Although we note that these two lines share an upper Hydrogen atomic level, complicated dependences of the respective combination coefficients on density and temperature distributions of the BLR gas might be a contributing factor to the different emission regions (e.g., Osterbrock & Ferland 2006, Chap. 4). In subsequent analysis, we therefore use two independent sets of parameters to describe the  $H\beta$  and  $Pa\alpha$  BLRs, except that they share the inclination and central black hole mass.

## 3. BROAD-LINE REGION MODELING

### 3.1. Basic Assumptions

Before constructing BLR models, we elaborate on necessary *ansatzs* for the sake of simplifying calculations:

- BLRs are composed of a large number of discrete, point-like clouds, which move in the gravitational well of the central black hole and reprocess the central ionizing emissions to line emissions with light-travel delays. Any shadowing among clouds is neglected (Pan-coast et al. 2014a).
- BLRs are stable in both structure and kinematics during the period under consideration, that is to say, all variability in emission lines are a result of reprocessing continuum variability so that RM is right applicable. The BLR “breathing” effects are not included (e.g., Cackett & Horne 2006) considering the mild fractional variability  $\lesssim 10\%$  of the  $5100 \text{ \AA}$  continuum and  $H\beta$  line for 3C 273 (Zhang et al. 2019). This is also supported by the almost unchanged  $H\beta$  and  $Pa\alpha$  profiles over more than a decade as illustrated in Figure 2.

- The central ionizing source is compact and has a point-like geometry so that its emissions are isotropic. The ionizing continuum is not available and the optical continuum is used as a substitute by assuming that the two bands of continuum emissions are linearly correlated with a negligible inter-delay (compared to the time delays of BLRs). The assumption of a linear correlation would be reasonable provided that the spectral energy distribution of the ionizing source received by BLR clouds does not change significantly.
- Detailed gas physics (such as photoionization) are not included and each cloud's emissions are simply proportional to the incident continuum fluxes with a nonlinear parameterization (see also Li et al. 2013). Specifically, this means that changes in line emissivity  $\epsilon(t)$  is related to changes in incident continuum flux  $f_c(t)$  for clouds at a radius  $r$  with a time delay  $\tau$

$$\frac{\dot{\epsilon}(r, t)}{\epsilon(r, t)} = (1 + \delta) \frac{\dot{f}_c(r, t)}{f_c(r, t)} = (1 + \delta) \frac{\dot{F}_c(t - \tau)}{F_c(t - \tau)}, \quad (1)$$

where the dot symbol represents the derivative with respect to time,  $F_c$  represents the continuum luminosity received by an observer, and  $\delta$  is the non-linear response parameter, which generally is a function of radius  $r$  and time  $t$ . Here, we note that  $\delta$  is closely related to the responsivity by  $\eta = 1 + \delta$ , which is formally defined as a derivative of the local line emission with respect to the incident hydrogen ionizing photon flux (see, e.g., Korista & Goad 2004; Goad & Korista 2014). We assume that  $\delta$  is a constant temporally and spatially, as a result,

$$\epsilon(r, t) \propto F_c^{1+\delta}(t - \tau). \quad (2)$$

Accordingly, the responsivity is also a constant temporally and spatially.

- All clouds rotate “coherently” around the central SMBH. Here we use “coherently” in the sense that each cloud's angular momentum is diverse but overall has a component oriented toward a common direction, i.e., the global rotation axis of the BLR. Such coherent rotation is crucial for SA signals because orbital motion with fully random angular momentum would result in null SA signals (e.g., G18; Songsheng et al. 2019).

Below we first introduce mathematical preliminaries for RM and SA analysis and then present our BLR dynamical models to calculate RM and SA signals.

## 3.2. Mathematical Preliminaries

### 3.2.1. Reverberation Mapping

Under the scenario that BLRs are composed of discrete clouds, the total line emissions are given by summing up all

clouds' emissions

$$F_l(v, t) = \sum_i \delta_D(v - v_i) \epsilon_i(t) = \sum_i \delta_D(v - v_i) A_i F_c^{1+\delta}(t - \tau_i), \quad (3)$$

where  $\delta_D(x)$  is the Dirac Delta function,  $A_i$  is the response coefficient, and  $v_i$  is the LOS velocity of  $i$ -th cloud. Because  $\delta$  is assumed to be a constant independent on clouds' location, we can rewrite the above equation into a general form as (e.g., Blandford & McKee 1982; Peterson 1993)

$$F_l(v, t) = \int \Psi_e(v, \tau) F_c^{1+\delta}(t - \tau) d\tau, \quad (4)$$

where the transfer function  $\Psi_e(v, \tau)$  is defined by

$$\Psi_e(v, \tau) = \sum_i \delta_D(v - v_i) \delta_D(\tau - \tau_i) A_i, \quad (5)$$

which measures the response of BLRs at LOS velocity  $v$  and time delay  $\tau$  and the subscript “ $e$ ” means emissivity weighting, to be distinguished from responsivity weighting defined below.

For small continuum variations, we can use the first-order Taylor expansions to approximate each cloud's emissions as

$$\begin{aligned} \epsilon_i(t) &= A_i [\bar{F}_c + \Delta F_c(t - \tau_i)]^{1+\delta} \\ &\approx A_i \bar{F}_c + (1 + \delta) A_i \Delta F_c(t - \tau_i), \end{aligned} \quad (6)$$

where  $\bar{F}_c$  represents the mean continuum flux and  $\Delta F_c$  represents the variations. By defining

$$\Delta F_l(v, t) = F_l(v, t) - \bar{F}_l(v), \quad \bar{F}_l(v) = \sum_i A_i \delta_D(v - v_i) \bar{F}_c, \quad (7)$$

we have

$$\Delta F_l(v, t) = \int \Psi_r(v, \tau) \Delta F_c(t - \tau) d\tau, \quad (8)$$

where

$$\Psi_r(v, \tau) = \sum_i (1 + \delta) A_i \delta_D(v - v_i) \delta_D(\tau - \tau_i), \quad (9)$$

and the subscript “ $r$ ” means responsivity weighting.

Equations (5) and (9) illustrate two branches of transfer functions widely used in the literature. The major difference is that there is an extra responsivity factor  $1 + \delta$  in Equation (9). Since  $\delta$  is a constant, emissivity-weighted and responsivity-weighted transfer functions are indeed identical. However, when  $\delta$  is no longer constant spatially, these two transfer functions will be different and give rise to different centroid time lags (see also Goad et al. 1993).

### 3.2.2. Spectroastrometry

SA measures astrometry, namely, emissivity-weighted photocenters, as a function of LOS velocity  $v$  at a specific time  $t$  (Beckers 1982; Bailey 1998),

$$\Theta_l(v, t) = \frac{1}{D_A} \frac{\sum_i \mathbf{x}_i \epsilon_i(t) \delta_D(v - v_i)}{\sum_i \epsilon_i(t) \delta_D(v - v_i)}, \quad (10)$$

where  $\mathbf{x}_i$  is projected position of  $i$ -th cloud on the sky and  $D_A$  is the angular size distance of the source. If we define the momentum of clouds' emissivity as

$$\mathbf{M}_l(v, t) = \sum_i \mathbf{x}_i \epsilon_i(t) \delta_D(v - v_i) \quad (11)$$

and the momentum transfer function as

$$\mathbf{\Pi}(v, \tau) = \sum_i \mathbf{x}_i \epsilon_i(t) \delta_D(v - v_i) \delta_D(\tau - \tau_i) A_i, \quad (12)$$

we have reverberation mapping of the momentum

$$\mathbf{M}_l(v, t) = \int \mathbf{\Pi}(v, \tau) F_c^{1+\delta}(t - \tau) d\tau. \quad (13)$$

The photocenters in Equation (10) can be rewritten into

$$\boldsymbol{\Theta}_l(v, t) = \frac{1}{D_A} \frac{\mathbf{M}_l(v, t)}{F_l(v, t)}. \quad (14)$$

In practice, there are two facts need to consider. First, the intensity we observed always consists of two components: one from the continuum and the other from the BLR. The continuum also contributes to the observed photocenters. As a result, the observed photocenters are indeed given by

$$\boldsymbol{\Theta}_{\text{all}}(v, t) = \frac{F_c(t) \boldsymbol{\Theta}_c(t) + F_l(v, t) \boldsymbol{\Theta}_l(v, t)}{F_c(t) + F_l(v, t)}. \quad (15)$$

It is reasonable to presume that the photocenters of the continuum do not change with wavelength/velocity. Therefore, we can use differential photocenters with respect to these of the continuum to further simplify calculations

$$\begin{aligned} \Delta \boldsymbol{\Theta}_{\text{all}}(v, t) &= \boldsymbol{\Theta}_{\text{all}}(v, t) - \boldsymbol{\Theta}_c(v, t) \\ &= \frac{f(v, t)}{1 + f(v, t)} \Delta \boldsymbol{\Theta}_l(v, t), \end{aligned} \quad (16)$$

where  $f(v, t)$  is the normalized line profile by the underlying continuum

$$f(v, t) = \frac{F_l(v, t)}{F_c(t)}, \quad (17)$$

and

$$\Delta \boldsymbol{\Theta}_l(v, t) = \boldsymbol{\Theta}_l(v, t) - \boldsymbol{\Theta}_c(v, t). \quad (18)$$

Second, we usually measure astrometry only along a specific direction, e.g., a slit's spatial direction through a spectrometer (e.g., Stern et al. 2015) or a baseline's direction through an interferometer (e.g., Gravity Collaboration et al. 2018). This effectively projects  $\boldsymbol{\Theta}_l(v, t)$  to a direction  $\mathbf{j}$  as

$$\theta_l(v, t) = \mathbf{j} \cdot \boldsymbol{\Theta}_l(v, t). \quad (19)$$

For interferometric observations, the observables are differential phases, related to photocenters as

$$\Delta \phi(v, t) = -2\pi \frac{\mathbf{B}}{\lambda} \cdot \boldsymbol{\Theta}_l(v, t), \quad (20)$$

where  $\mathbf{B}$  is the baseline and  $\lambda$  is the wavelength, related to the velocity by  $v/c = [\lambda/(1+z) - \lambda_0]/\lambda_0$ , where  $c$  is the speed of light and  $\lambda_0$  is the rest wavelength of the emission line.

In an extreme example where the continuum pulsars at time  $t_0$ , namely,  $F_c^{1+\delta}(t) \sim \delta_D(t - t_0)$ , we have the line emissions, momentum transfer function, and photocenters as

$$F_l(v, t) = \Psi_e(v, t - t_0), \quad (21)$$

$$\mathbf{M}_l(v, t) = \mathbf{\Pi}(v, t - t_0), \quad (22)$$

$$\Delta \boldsymbol{\Theta}_{\text{all}}(v, t) = \frac{1}{D_A} \frac{f(v, t)}{1 + f(v, t)} \frac{\mathbf{\Pi}(v, t - t_0)}{\Psi_e(v, t - t_0)}, \quad (23)$$

where we neglect the photocenters of the continuum. Conversely, if the continuum flux is constant, the line emissions, momentum transfer function, and photocenters are time independent accordingly,

$$F_l(v) = \Psi_e(v) \bar{F}_c, \quad (24)$$

$$\mathbf{M}_l(v) = \mathbf{\Pi}(v) \bar{F}_c, \quad (25)$$

$$\Delta \boldsymbol{\Theta}_{\text{all}}(v) = \frac{1}{D_A} \frac{f(v)}{1 + f(v)} \frac{\mathbf{\Pi}(v)}{\Psi_e(v)}, \quad (26)$$

where  $\Psi_e(v)$  and  $\mathbf{\Pi}(v)$  are delay integral of  $\Psi_e(v, \tau)$  and  $\mathbf{\Pi}(v, \tau)$ , respectively. Here, again, the photocenters of the continuum are neglected.

Equation (14) implies that SA signals of BLRs are generally a function of time owing to responses of the emission line to the continuum variability. For 3C 273, the H $\beta$  light curve is almost invariable during the period (July, 2017-May, 2018) of SA observations. We expect a similar property for the Pa $\alpha$  line, therefore, we neglect time dependences of the SA signals and directly use Equations (24-26) to fit the observed SA data.

### 3.3. Broad-line Region Models

We now proceed to construct phenomenological BLR dynamical models based on the framework of Pancoast et al. (2014a) and Li et al. (2018). Section 3.2 demonstrates that to calculate RM and SA signals, we need to specify geometry, dynamics, and emissivity of BLR clouds.

#### 3.3.1. Geometry

Based on previous 2D RM observations (e.g., Denney et al. 2010; Grier et al. 2013; Du et al. 2016, 2018; Lu et al. 2016; De Rosa et al. 2018; see also a review of Peterson 2014), BLR clouds are assumed to follow a disk-like, axisymmetric geometry. The BLR is viewed at an inclination angle  $\theta_{\text{inc}}$  and subtends an opening angle  $\theta_{\text{opn}}$ . Here,  $\theta_{\text{inc}}$  is defined to be the angle between the LOS and the symmetry axis of the BLR;  $\theta_{\text{opn}}$  is defined as such that  $\theta_{\text{opn}} = 90^\circ$  produces a spherical BLR while  $\theta_{\text{opn}} = 0^\circ$  produces an infinitely thin disk-like BLR (see the schematic Figure 1 of Li et al. 2013).

In the radial direction, we adopt two types of distributions to assign clouds' distances from the central black hole, as shown in the top panels of Figure 3.

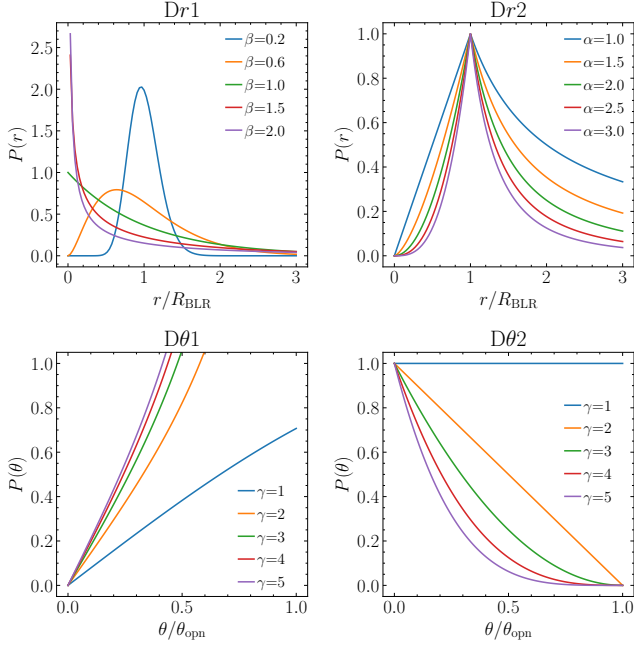


**Figure 3.** Adopted distributions of BLR clouds along (top) radial and (bottom) vertical directions. See Section 3.3.1 for the detail.

**Dr1**—The distribution is parameterized by a gamma distribution (Pancoast et al. 2014a). A BLR cloud is assigned a location by

$$r = F_{\text{in}} R_{\text{BLR}} + (1 - F_{\text{in}}) \mathcal{R}, \quad (27)$$

where  $F_{\text{in}}$  is a fraction to denote the inner edge of the BLR and  $\mathcal{R}$  is a random number generated from a gamma distribution with a mean  $R_{\text{BLR}}$  and a standard deviation  $\beta R_{\text{BLR}}$ . Here, the gamma distribution has a form of

$$P(x|a, s) = \frac{x^{a-1}}{\Gamma(a)s^a} \exp\left(-\frac{x}{s}\right), \quad (28)$$

where  $a$  is the shape parameter,  $s$  is the scale parameter,  $\Gamma(a)$  is the Gamma function. In our parameterization,  $a = 1/\beta^2$  and  $s = \beta^2 R_{\text{BLR}}$ .

**Dr2**—The distribution is parameterized by a double power law (Stern et al. 2015; Li et al. 2018) as

$$P(r) \propto \begin{cases} (r/R_{\text{BLR}})^\alpha & \text{for } F_{\text{in}} \leq r/R_{\text{BLR}} \leq 1, \\ (r/R_{\text{BLR}})^{-\alpha} & \text{for } 1 \leq r/R_{\text{BLR}} \leq F_{\text{out}}, \end{cases} \quad (29)$$

where  $\alpha$  is the slope of power law, and  $F_{\text{in}}$  and  $F_{\text{out}}$  are parameters that control the inner and out radius.

In the  $\theta$ -direction, we also adopt two types of distributions as follows (see the bottom panels of Figure 3).

**Dθ1**—A distribution inclined to the outer faces of the BLR disk (Pancoast et al. 2014a)

$$\theta = \cos^{-1} [\cos \theta_{\text{opn}} + (1 - \cos \theta_{\text{opn}}) \times U^\gamma], \quad (30)$$

where  $\gamma$  is a free parameter to control to which extent clouds are clustered close to the outer faces and  $U$  is a uniformly distributed random number between 0 and 1. This produces a distribution density

$$P(\theta) \propto \sin \theta (\cos \theta - \cos \theta_{\text{opn}})^{-(\gamma-1)/\gamma}. \quad (31)$$

The case of  $\gamma = 1$  results in a uniform distribution of BLR clouds in terms of  $\cos \theta$ .

**Dθ2**—A distribution inclined to the equatorial plane of the BLR disk

$$\theta = \theta_{\text{opn}} \times (1 - U^{1/\gamma}), \quad (32)$$

which produces a distribution density

$$P(\theta) \propto (1 - \theta/\theta_{\text{opn}})^{\gamma-1}. \quad (33)$$

The case of  $\gamma = 1$  gives a uniform distribution of BLR clouds in the  $\theta$ -direction.

We note that the above radial and vertical distributions are purely phenomenological. There are not yet observations that directly constrain the most appropriate distributions. We introduce these distributions to test for model dependence of our results.

### 3.3.2. Dynamics

The prescription for BLR dynamics in Pancoast et al. (2014a)’s phenomenological model is flexible to cover Keplerian motion, inflows and outflows. We directly use this prescription and outline the essentials below for the sake of completeness.

In this prescription, a fraction  $f_{\text{ellip}}$  of clouds have bound elliptical Keplerian orbits and the remaining fraction  $1 - f_{\text{ellip}}$  is in either inflowing ( $0 < f_{\text{flow}} < 0.5$ ) or outflowing ( $0.5 < f_{\text{flow}} < 1$ ). Each cloud’s velocities are first assigned in its orbital plane and then converted into three-dimensional velocities through appropriate coordinate transformations. For elliptical orbits, the radial and tangential velocities are drawn from Gaussian distributions centered around a point  $(v_r, v_\phi) = (0, v_{\text{circ}})$  with standard deviations  $\sigma_{\rho, \text{circ}}$  and  $\sigma_{\Theta, \text{circ}}$ , respectively. Here,  $v_{\text{circ}} = \sqrt{GM_\bullet/r}$  is the local Keplerian velocity. For inflowing/outflowing clouds, velocities are drawn similarly from Gaussian distributions centered around points  $(v_r, v_\phi) = (\pm\sqrt{2}v_{\text{circ}}, 0)$  with standard deviations  $\sigma_{\rho, \text{rad}}$  and  $\sigma_{\Theta, \text{rad}}$ , where “+” corresponds to outflows and “−” corresponds to inflows. It is straightforward to verify that a half of such generated inflows/outflows have bound orbits. To account for completely bound inflowing and outflowing orbits, the Gaussian distributions are allowed to rotate by an angle  $\theta_e$  along the ellipse that has a semiminor axis  $v_{\text{circ}}$  in the  $v_\phi$  direction and a semimajor axis  $\sqrt{2}v_{\text{circ}}$  in the  $v_r$  direction (see Figure 2 in Pancoast et al. 2014a). Finally, all clouds’ tangential velocities are forced to have the same sign (say, e.g., positive) so as to maintain the overall coherent rotation (see Section 3.1).

An extra small velocity offset is added to the LOS velocity to account for macroturbulences as

$$v_{\text{turb}} = \mathcal{N}(0, \sigma_{\text{turb}})v_{\text{circ}}, \quad (34)$$

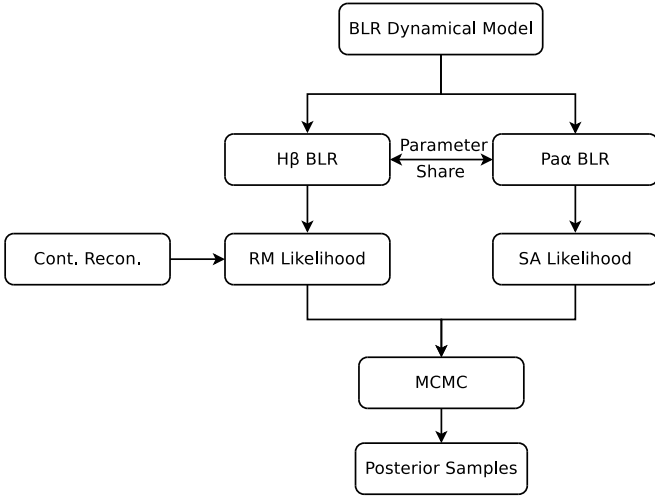


**Figure 4.** A schematic diagram of the joint analysis of SA and RM observations for 3C 273. The  $H\beta$  BLR and  $\text{Pa}\alpha$  BLR share inclination and black hole mass (see the text).

where  $\mathcal{N}(0, \sigma_{\text{turb}})$  is a random number generated from a normal distribution with a standard deviation of  $\sigma_{\text{turb}}$ .

### 3.3.3. Emissivity

The clouds' emissivity is set according to Equation (2). To account for the possibility that BLR clouds are optically thick so that their emissions are anisotropic, we assign a weight to each cloud using a prescription (Blandford & McKee 1982)

$$w = \frac{1}{2} + \kappa \cos \phi, \quad (35)$$

where  $\kappa$  is a parameter in the range  $(-1/2, 1/2)$  and  $\phi$  is the angle between the observer's and cloud's LOS to the central black hole. A negative  $\kappa$  corresponds to emissions preferentially from the far side of BLR clouds and a positive  $\kappa$  corresponds to emissions preferentially from the near side.

In addition, there is a possibility for some obscuring material in the equatorial plane that may not be transparent to BLR clouds located below the equatorial plane. Following Pancoast et al. (2014a), we define a parameter  $\xi$  to describe this effect. For  $\xi = 0$ , the entire half of the BLR below the equatorial plane is completely obscured; while for  $\xi = 1$ , the equatorial plane becomes transparent so that the half can be directly observed.

### 3.4. Continuum Modeling and Long-term Detrending

We use the optical continuum light curve of 3C 273 compiled by Li et al. (2020), which synthesized the data from the All-Sky Automated Survey for Supernovae project (Kochanek et al. 2017), the Small and Moderate Aperture Research Telescope System monitoring program (Bonning et al. 2012), *Swift* archives as well as from Zhang et al. (2019). We employ a damped random walk process to describe the continuum variability, which allows us to interpolate and extrapolate the observed continuum light curve at a given time

grid (Pancoast et al. 2014a; Li et al. 2018). A damped random walk process is described by two parameters  $\tau_d$  and  $\sigma_d$ , which represent the characteristic timescale of variations variation amplitude and the standard deviation of variations on long-timescale ( $\gg \tau_d$ ), respectively. For an observed light curve, a reconstruction is obtained by starting with the best estimators at the given time grid and adding them Gaussian processes. The parameters  $\tau_d$  and  $\sigma_d$  together with the Gaussian processes are further constrained by fitting the emission line data (see Pancoast et al. 2014a and Li et al. 2018 for the detail).

For 3C 273, an additional detrending treatment must be taken into account. The continuum light curve shows a distinct long-term trend that does not have a corresponding echo in the  $H\beta$  light curve (Zhang et al. 2019; Li et al. 2020). 3C 273 is a flat-spectrum radio quasar with both comparably prominent jet and accretion disk emissions in its broadband spectral energy distribution. As summarized in Li et al. (2020), several pieces of evidence clearly demonstrated that the optical emissions of 3C 273 are composed of two components, one from the accretion disk and the other from the jet contribution. The most conclusive evidence come from the *Swift* UV light curve of 3C 273, which is remarkably coincident with the scaled  $H\beta$  light curve after correcting for the time delay (see Figure 2 in Li et al. 2020) but distinct from the optical continuum light curve in the long-term trend. The jet contributions can naturally explain the non-echoed long-term trend in the continuum light curve. Li et al. (2020) succeeded in detrending the continuum light curve using the radio light curve, which is generally consistent with the simple detrending using a linear polynomial.

In this work, we use the both approaches to detrend the continuum light curve. For the approach of linear detrending, to keep the mean flux of the continuum light curve unchanged, we only need one free parameter to delineate the slope of the linear polynomial, namely,

$$F_c(t) = F'_c(t) - a(t - t_{\text{med}}), \quad (36)$$

where  $F'_c(t)$  is the original continuum light curve,  $a$  is the slope of the linear polynomial and  $t_{\text{med}}$  is the median time of the continuum light curve. For the approach of detrending with a radio light curve, we use the radio data from the large-scale, fast-cadence 15 GHz monitoring program with the 40 m telescope at the Owens Valley Radio Observatory (Richards et al. 2011). The detrended light curve is given by

$$F_c(t) = F'_c(t) - a_r [F_r(t - \tau_r) - b_r], \quad (37)$$

where  $F_r$  is the radio light curve,  $\tau_r$  is the time delay between the radio and continuum light curves, and  $a_r$  and  $b_r$  are free parameters. Because the radio light curve has intense sampling (nearly a daily cadence), we simply use the linear interpolation to derive the radio flux at a given time. We note that Li et al. (2020) adopted a more sophisticated detrending scheme, in which the radio light curve is regarded as a blurred echo of the optical light curve of the jet with a Gaussian transfer function. The inferred standard deviation of the

**Table 1.** BLR Models with Combinations of Different Radial and Vertical Profiles of BLR Clouds and Continuum Detrending Approaches.

Model	Radial Profile	Vertical Profile	Continuum Detrending
M1	D <i>r</i> 1	Dθ1	Linear
M2	D <i>r</i> 1	Dθ2	Linear
M3	D <i>r</i> 2	Dθ1	Linear
M4	D <i>r</i> 2	Dθ2	Linear
M5	D <i>r</i> 1	Dθ1	Radio
M6	D <i>r</i> 1	Dθ2	Radio
M7	D <i>r</i> 2	Dθ1	Radio
M8	D <i>r</i> 2	Dθ2	Radio

NOTE—“Linear” and “radio” denote long-term detrending of the continuum using a linear polynomial and the radio light curve, respectively (see Section 3.4).

Gaussian was about 13 days. It will significantly magnify the computation time to incorporate the scheme of Li et al. (2020) into present framework. Therefore, we prefer to the above simple treatment in Equation (37). Nevertheless, our treatment in Equation (37) is equivalent to using an infinitesimally narrow Gaussian, which is reasonable considering the quite narrow Gaussian width obtained by Li et al. (2020).

### 3.5. A Suite of Models

In Section 3.3.1, we introduce two radial distributions and two vertical distributions for BLR clouds. Also, there are two approaches to detrend the continuum light curve (see Section 3.4). With these ingredients, we have 8 different combinations for BLR models, as summarized in Table 1. In each model, the Hβ and Paα BLRs have the same parameterization and share the inclination angle ( $\theta_{\text{inc}}$ ) and black hole mass ( $M_{\bullet}$ ). As such, we can test how the obtained results depend on specific BLR models and justify the most probable model. We note that those models (M1 and M5) with a combination of D*r*1 and Dθ1 are identical to Pancoast et al. (2014a)’s BLR model.

In the calculations, we use  $10^6$  particles to represent BLR clouds and set the maximum radius of BLR clouds fixed to 800 lt-days, which is equal to the characteristic radius of the dusty torus in 3C 273 (Gravity Collaboration et al. 2020b). Since the bulk of line emissions come from much smaller regions, this fixed outer radius does not influence the results. Our following calculations also confirmed that the finally obtained mean BLR sizes are smaller than this outer radius. This is as expected because the Hβ time delay with respect to the continuum variations is around 150 days (Zhang et al. 2019; Li et al. 2020) and the Paα BLR sizes also should not be much larger than the Hβ BLR size in consideration of their line widths (see Figure 12).

## 4. JOINT BAYESIAN ANALYSIS

### 4.1. Bayesian Inference

In Figure 4, we show a schematic diagram of the joint analysis between SA and RM observation data for 3C 273. Given a BLR dynamical model, we generate positions and velocities of clouds for the Hβ and Paα BLRs, which share the parameters of inclination and black hole mass. We then separately calculate simulated RM data (namely, a time series of Hβ spectra) and SA data (including Paα profile and differential phases). The simulated Hβ spectra further need reconstructed continuum time series as a prior input. By comparing against the observation data ( $\mathbf{D}_{\text{RM}}, \mathbf{D}_{\text{SA}}$ ), we obtain the corresponding likelihoods given a model parameter set  $\theta$ . The likelihood for RM data is given by

$$P(\mathbf{D}_{\text{RM}}|\theta) = \prod_{ij} \frac{1}{\sqrt{2\pi}\sigma_{f,ij}} \exp \left\{ -\frac{[f_{ij} - f_{ij}^m(\theta|F_c)]^2}{2\sigma_{f,ij}^2} \right\}, \quad (38)$$

where  $f_{ij}$  and  $\sigma_{f,ij}$  represent the observed flux density and uncertainty of the Hβ line at  $i$ -th epoch and  $j$ -th velocity bin, respectively, and  $f_{ij}^m(\theta)$  represents the modeled flux density, which depends on the observed continuum light curve  $F_c$ . The likelihood for SA data is given by

$$P(\mathbf{D}_{\text{SA}}|\theta) = \prod_i \frac{1}{\sqrt{2\pi}\sigma_{F,i}} \exp \left\{ -\frac{[F_i - F_i^m(\theta)]^2}{2\sigma_{F,i}^2} \right\} \\ \times \prod_{ij} \frac{1}{\sqrt{2\pi}\sigma_{\phi,ij}} \exp \left\{ -\frac{[\phi_{ij} - \phi_{ij}^m(\theta)]^2}{2\sigma_{\phi,ij}^2} \right\} \quad (39)$$

where  $F_i$  and  $\sigma_{F,i}$  represent the observed flux density and uncertainty of the Paα line at the  $i$ -th velocity bin,  $\phi_{ij}$  and  $\sigma_{\phi,ij}$  represent the observed differential phase and uncertainty at  $i$ -th velocity bin and  $j$ -th baseline,  $F_i^m$  and  $\phi_{ij}^m$  represent the modeled flux density and differential phase, respectively.

Based on the Bayes’ theorem, the posterior probability is

$$P(\theta|\mathbf{D}_{\text{SA}}, \mathbf{D}_{\text{RM}}) = \frac{P(\mathbf{D}_{\text{SA}}|\theta)P(\mathbf{D}_{\text{RM}}|\theta)P(\theta)}{P(\mathbf{D}_{\text{SA}}, \mathbf{D}_{\text{RM}})}, \quad (40)$$

where  $P(\theta)$  is the prior of parameters and  $P(\mathbf{D}_{\text{SA}}, \mathbf{D}_{\text{RM}})$  is the Bayesian evidence. Table 2 summarizes the major parameters of BLR models and their prior ranges. We use the Markov-chain Monte Carlo (MCMC) technique along with the diffusive nested sampling algorithm (Brewer et al. 2011) to explore the posterior probability. The diffusive nested sampling algorithm calculates Bayesian evidence inherently (Sivia & Skilling 2006) and performs well in high-dimensional and multimodal distributions (Brewer & Forman-Mackey 2018).

Following Li et al. (2018), to account for any possible unknown errors in spectral reduction and decomposition, we include an extra parameter  $s_{\text{RM}}$  to magnify the errors of the Hβ profile data as  $\sigma^2 = \sigma_d^2 + s_{\text{RM}}^2 \bar{\sigma}_d^2$ , where  $\sigma_d$  is the data errors and  $\bar{\sigma}_d$  is the averaged error of all the Hβ profiles. We adopt a prior of  $P(x) = 1/(1+x)$  for  $s_{\text{RM}}$ , which behaves like a uniform prior when  $s_{\text{RM}} \ll 1$  and like a logarithm prior when  $s_{\text{RM}} \gg 1$  (Gregory 2011). The prior range is set to (0, 10).

**Table 2.** Major Parameters for BLR Models.

Parameter	Prior	Range	Unit	Implication
$M_{\bullet}$	LogUniform	$(10^6, 10^{10})$	$M_{\odot}$	Black hole mass
$D_{\Delta}$	LogUniform	$(10, 5 \times 10^3)$	Mpc	Angular-size distance
$\theta_{\text{inc}}$	CosUniform	$(0, 60)$	deg	Inclination angle
PA	Uniform	$(-180, 180)$	deg	Position angle on the sky (east of north)
$R_{\text{BLR}}$	LogUniform	$(10, 400)$	lt-day	Mean BLR radius ( $Dr1$ )
$\beta$	Uniform	$(0, 2)$	...	Unit standard deviation of radial gamma distribution ( $Dr1$ )
$F_{\text{in}}$	Uniform	$(0, 1)$	...	Inner edge in units of $R_{\text{BLR}}$ ( $Dr1$ and $Dr2$ )
$F_{\text{out}}$	LogUniform	$(1, 100)$	...	Outer edge in units of $R_{\text{BLR}}$ ( $Dr2$ )
$\alpha$	Uniform	$(1, 3)$	...	Slope of the power-law radial distribution
$\theta_{\text{open}}$	Uniform	$(0, 90)$	deg	Opening angle
$\kappa$	Uniform	$(-0.5, 0.5)$	...	Anisotropy of the cloud emission
$\gamma$	Uniform	$(1, 5)$	...	Clustering of clouds in the vertical direction
$\xi$	Uniform	$(0, 1)$	...	Transparency of the equatorial material
$f_{\text{ellip}}$	Uniform	$(0, 1)$	...	Fraction of bound elliptical orbits
$f_{\text{flow}}$	Uniform	$(0, 1)$	...	Flag for determining inflowing or outflowing orbits

NOTE—“Uniform” denotes a uniform prior, “LogUniform” denotes a uniform prior for the logarithm of the parameter, and “CosUniform” denotes a uniform prior for the cosine of the parameter.

We incorporate the above joint analysis procedure into our previous developed package BRAINS (Li et al. 2018), which is publicly available at <https://github.com/LiyAstroph/BRAINS>. The package was written in C language and runs on parallel computer clusters with the standardized message passing interface based on a diffusive nested sampling library CDNEst (Li 2020). For each model, we implement the sampling algorithm to generate 40000 “raw” parameter samples, from which the final posterior samples are derived based on the recorded sampling information (such as the likelihood levels and associated prior mass). The convergence of the sampling is checked by inspecting the distribution of posterior weights as a function of prior mass. To be specific, good sampling will see a significant peak in the distribution, which implies that the important parameter space where posterior weights get maximum is appropriately captured (see Brewer et al. 2011 for a detail). A posterior temperature ( $T$ ) is introduced to anneal the likelihoods when deriving the posterior samples (see also Pancoast et al. 2014a). We use temperatures of 5-15 for the 8 models. We finally determine the best estimates of parameters and their uncertainties by the medians of the corresponding posterior distributions and the 68.3% confidence intervals, respectively.

#### 4.2. Model Selection

Among the 8 BLR models, we employ the Bayes factor to select the most probable one. The Bayes factor of two models, e.g., say M1 and M2, is defined by the ratio of their posterior probabilities and quantifies the relative merits of the two models. As usual, we assign equal priors for the two models. In this case, the Bayes factor is equal to the ratio of the Bayesian evidence (e.g., Sivia & Skilling 2006)

$$K = \frac{P(M2|\mathbf{D}_{\text{SA}}, \mathbf{D}_{\text{RM}})}{P(M1|\mathbf{D}_{\text{SA}}, \mathbf{D}_{\text{RM}})} = \frac{P(\mathbf{D}_{\text{SA}}, \mathbf{D}_{\text{RM}}|M2)}{P(\mathbf{D}_{\text{SA}}, \mathbf{D}_{\text{RM}}|M1)}. \quad (41)$$

A Bayes factor  $K > 1$  means that M2 is relatively preferable. A conventional threshold for a decisive preference is  $K > 100$  (Jeffreys 2003).

There are otherwise independent observations that can aid us in model selection. First, 3C 273 displays a prominent radio jet (e.g., Courvoisier 1998). The viewing inclination measured through superluminal motion ranges from  $3.8^\circ$  to  $\sim 15^\circ$  (Lobanov & Zensus 2001; Savolainen et al. 2006; Meyer et al. 2016; Jorstad et al. 2017). This provides a useful constraint if assuming an alignment between the rotation axis of the BLR and the jet. Second, there are well-established correlations between black hole mass and luminosity/mass of classical bulges and ellipticals (see, e.g., Kormendy & Ho 2013). Using the *Hubble Space Telescope*/WFC3 images, Zhang et al. (2019) derived the bulge mass  $\log(M_{\text{bulge}}/M_{\odot}) = 11.3 \pm 0.7$  and  $K$ -band bulge luminosity<sup>5</sup>  $\log(L_{K,\text{bulge}}/L_{K\odot}) = 11.68 \pm 0.28$ , where  $L_{K\odot}$  is the  $K$ -band luminosity of the Sun. We can compare our obtained black hole mass against these correlations to justify the most probable model based on the Bayes factor.

## 5. RESULTS

### 5.1. Overview

In Table 3, we summarize the inferred values and uncertainties of major parameters for the 8 BLR models listed in Table 1. We also calculate the maximum likelihood  $\ln \mathcal{L}_{\text{max}}$  and the Bayes factor  $\ln K$  for each model and tabulate their values with respect to model M1 in Table 3. The most probable model in light of both  $\ln \mathcal{L}_{\text{max}}$  and Bayes factor is M4, which has the maximum  $\ln \mathcal{L}_{\text{max}}$  and  $\ln K$ . In model M4,

<sup>5</sup> Note that here, we use a cosmology of  $H_0 = 70.5 \text{ km s}^{-1} \text{ Mpc}^{-1}$  for consistency with Kormendy & Ho (2013).

**Table 3.** Inferred Model Parameters.

Model	M1	M2	M3	M4	M5	M6	M7	M8
$\log(M_{\bullet}/10^8 M_{\odot})$	$0.10^{+0.40}_{-0.33}$	$0.46^{+0.51}_{-0.28}$	$0.21^{+0.24}_{-0.26}$	$1.06^{+0.21}_{-0.27}$	$-0.04^{+0.25}_{-0.29}$	$0.46^{+0.53}_{-0.57}$	$0.16^{+0.13}_{-0.25}$	$0.79^{+0.36}_{-0.48}$
$\log(D_{\Lambda}/\text{Mpc})$	$3.09^{+0.23}_{-0.23}$	$2.61^{+0.39}_{-0.30}$	$3.14^{+0.17}_{-0.22}$	$2.83^{+0.32}_{-0.28}$	$2.94^{+0.29}_{-0.31}$	$2.71^{+0.35}_{-0.39}$	$3.12^{+0.18}_{-0.19}$	$2.62^{+0.34}_{-0.30}$
$\theta_{\text{inc}}$	$30^{+10}_{-11}$	$8^{+1}_{-3}$	$29^{+7}_{-11}$	$5^{+1}_{-1}$	$31^{+9}_{-11}$	$9^{+6}_{-3}$	$32^{+6}_{-9}$	$7^{+2}_{-2}$
PA/deg	$192^{+20}_{-27}$	$190^{+32}_{-41}$	$196^{+18}_{-24}$	$196^{+32}_{-36}$	$193^{+22}_{-24}$	$197^{+22}_{-36}$	$196^{+19}_{-30}$	$202^{+20}_{-36}$
H $\beta$								
$\log(R_{\text{BLR}}/\text{lt-day})$	$2.10^{+0.14}_{-0.23}$	$2.07^{+0.22}_{-0.12}$	$1.15^{+0.14}_{-0.10}$	$1.83^{+0.43}_{-0.16}$	$1.93^{+0.21}_{-0.23}$	$1.92^{+0.34}_{-0.22}$	$1.15^{+0.12}_{-0.13}$	$1.60^{+0.35}_{-0.40}$
$\beta$	$1.62^{+0.10}_{-0.05}$	$1.58^{+0.16}_{-0.33}$	...	...	$1.63^{+0.10}_{-0.05}$	$1.74^{+0.13}_{-0.53}$	...	...
$F_{\text{in}}$	$0.10^{+0.01}_{-0.01}$	$0.14^{+0.07}_{-0.04}$	$0.36^{+0.39}_{-0.26}$	$0.34^{+0.40}_{-0.26}$	$0.10^{+0.01}_{-0.01}$	$0.11^{+0.12}_{-0.02}$	$0.28^{+0.22}_{-0.22}$	$0.41^{+0.42}_{-0.28}$
$\log F_{\text{out}}$	...	...	$1.64^{+0.06}_{-0.04}$	$0.98^{+0.14}_{-0.79}$	...	...	$1.63^{+0.03}_{-0.05}$	$1.20^{+0.31}_{-0.27}$
$\alpha$	...	...	$1.21^{+0.08}_{-0.03}$	$1.67^{+0.33}_{-0.54}$	...	...	$1.21^{+0.04}_{-0.03}$	$1.58^{+0.37}_{-0.26}$
$\theta_{\text{opn}}$	$35^{+11}_{-14}$	$75^{+11}_{-26}$	$31^{+8}_{-9}$	$78^{+4}_{-13}$	$34^{+11}_{-10}$	$72^{+11}_{-21}$	$36^{+6}_{-10}$	$77^{+11}_{-12}$
$\kappa$	$-0.13^{+0.35}_{-0.25}$	$0.07^{+0.14}_{-0.35}$	$0.10^{+0.31}_{-0.33}$	$-0.11^{+0.42}_{-0.28}$	$0.06^{+0.25}_{-0.47}$	$-0.21^{+0.52}_{-0.25}$	$0.23^{+0.18}_{-0.24}$	$0.05^{+0.30}_{-0.46}$
$\gamma$	$3.85^{+0.95}_{-1.69}$	$1.50^{+0.76}_{-0.38}$	$4.54^{+0.36}_{-1.10}$	$2.66^{+0.65}_{-0.42}$	$3.70^{+1.00}_{-1.59}$	$2.11^{+1.30}_{-0.94}$	$4.62^{+0.26}_{-0.67}$	$2.09^{+0.99}_{-0.74}$
$\xi$	$0.63^{+0.30}_{-0.32}$	$0.68^{+0.21}_{-0.36}$	$0.64^{+0.26}_{-0.18}$	$0.91^{+0.07}_{-0.64}$	$0.59^{+0.34}_{-0.27}$	$0.47^{+0.37}_{-0.34}$	$0.65^{+0.28}_{-0.30}$	$0.62^{+0.34}_{-0.41}$
$f_{\text{ellip}}$	$0.29^{+0.19}_{-0.19}$	$0.29^{+0.24}_{-0.24}$	$0.23^{+0.18}_{-0.14}$	$0.27^{+0.30}_{-0.17}$	$0.27^{+0.21}_{-0.20}$	$0.39^{+0.35}_{-0.29}$	$0.28^{+0.22}_{-0.20}$	$0.47^{+0.13}_{-0.25}$
$f_{\text{flow}}$	$0.30^{+0.31}_{-0.20}$	$0.28^{+0.21}_{-0.18}$	$0.29^{+0.18}_{-0.21}$	$0.31^{+0.26}_{-0.20}$	$0.32^{+0.22}_{-0.21}$	$0.32^{+0.30}_{-0.25}$	$0.24^{+0.18}_{-0.16}$	$0.34^{+0.39}_{-0.27}$
$\delta$	$-0.20^{+0.05}_{-0.05}$	$-0.19^{+0.05}_{-0.04}$	$-0.20^{+0.03}_{-0.03}$	$-0.14^{+0.05}_{-0.06}$	$-0.54^{+0.02}_{-0.02}$	$-0.54^{+0.03}_{-0.02}$	$-0.53^{+0.02}_{-0.02}$	$-0.51^{+0.03}_{-0.03}$
Pa $\alpha$								
$\log(R_{\text{BLR}}/\text{lt-day})$	$2.33^{+0.18}_{-0.23}$	$1.86^{+0.27}_{-0.22}$	$1.64^{+0.16}_{-0.19}$	$1.94^{+0.39}_{-0.32}$	$2.18^{+0.24}_{-0.26}$	$2.01^{+0.30}_{-0.37}$	$1.61^{+0.12}_{-0.18}$	$1.74^{+0.41}_{-0.37}$
$\beta$	$1.36^{+0.19}_{-0.20}$	$0.98^{+0.67}_{-0.69}$	...	...	$1.36^{+0.20}_{-0.18}$	$1.23^{+0.49}_{-0.67}$	...	...
$F_{\text{in}}$	$0.13^{+0.04}_{-0.04}$	$0.46^{+0.32}_{-0.25}$	$0.45^{+0.34}_{-0.34}$	$0.53^{+0.33}_{-0.34}$	$0.13^{+0.04}_{-0.04}$	$0.33^{+0.36}_{-0.19}$	$0.50^{+0.33}_{-0.32}$	$0.55^{+0.34}_{-0.34}$
$\log F_{\text{out}}$	...	...	$1.54^{+0.35}_{-0.32}$	$0.96^{+0.69}_{-0.54}$	...	...	$1.54^{+0.34}_{-0.32}$	$0.95^{+0.55}_{-0.57}$
$\alpha$	...	...	$1.17^{+0.17}_{-0.12}$	$2.22^{+0.50}_{-0.69}$	...	...	$1.17^{+0.13}_{-0.12}$	$2.16^{+0.55}_{-0.70}$
$\theta_{\text{opn}}$	$32^{+16}_{-13}$	$66^{+17}_{-23}$	$33^{+15}_{-9}$	$49^{+20}_{-14}$	$35^{+17}_{-13}$	$69^{+15}_{-30}$	$34^{+16}_{-9}$	$57^{+18}_{-16}$
$\kappa$	$0.04^{+0.25}_{-0.26}$	$-0.02^{+0.35}_{-0.30}$	$0.10^{+0.25}_{-0.34}$	$-0.01^{+0.35}_{-0.32}$	$0.06^{+0.28}_{-0.28}$	$0.02^{+0.28}_{-0.33}$	$0.12^{+0.22}_{-0.29}$	$0.03^{+0.28}_{-0.31}$
$\gamma$	$2.73^{+1.57}_{-1.17}$	$3.12^{+1.14}_{-1.02}$	$2.65^{+1.55}_{-1.18}$	$3.25^{+1.21}_{-1.09}$	$2.75^{+1.70}_{-1.24}$	$2.71^{+1.18}_{-1.07}$	$3.02^{+1.26}_{-1.50}$	$3.29^{+0.94}_{-1.12}$
$\xi$	$0.63^{+0.25}_{-0.35}$	$0.58^{+0.32}_{-0.34}$	$0.60^{+0.25}_{-0.31}$	$0.62^{+0.26}_{-0.39}$	$0.66^{+0.23}_{-0.42}$	$0.60^{+0.28}_{-0.45}$	$0.67^{+0.22}_{-0.38}$	$0.54^{+0.32}_{-0.28}$
$f_{\text{ellip}}$	$0.61^{+0.28}_{-0.36}$	$0.59^{+0.29}_{-0.35}$	$0.51^{+0.34}_{-0.31}$	$0.61^{+0.28}_{-0.39}$	$0.50^{+0.34}_{-0.32}$	$0.62^{+0.29}_{-0.35}$	$0.66^{+0.24}_{-0.45}$	$0.59^{+0.28}_{-0.41}$
$f_{\text{flow}}$	$0.43^{+0.35}_{-0.30}$	$0.45^{+0.35}_{-0.31}$	$0.41^{+0.34}_{-0.27}$	$0.57^{+0.30}_{-0.40}$	$0.45^{+0.36}_{-0.32}$	$0.49^{+0.38}_{-0.29}$	$0.47^{+0.35}_{-0.33}$	$0.58^{+0.32}_{-0.42}$
$s_{\text{RM}}$	3.760	3.515	3.675	3.335	3.571	3.685	3.540	3.532
$\chi^2_{\text{RM}}/N_{\text{RM}}$	0.985	0.986	0.985	0.986	1.039	0.987	1.034	1.012
$\chi^2_{\text{SA}}/N_{\text{SA}}$	1.304	1.326	1.378	1.401	1.344	1.309	1.329	1.317
$\ln \mathcal{L}_{\text{max}}$	0	61.71	17.15	105.45	14.34	17.65	26.23	42.12
$\ln K$	0	31.09	27.36	83.79	39.47	47.81	53.80	73.73

NOTE—The maximum likelihood  $\ln \mathcal{L}_{\text{max}}$  and Bayes factor  $\ln K$  are given with respect to model M1. The Bayes factor  $\ln K$  and  $\ln \mathcal{L}_{\text{max}}$  are given using a posterior annealing temperature of  $T = 8$  in the diffusive nested sampling algorithm. The values of  $s_{\text{RM}}$ ,  $\chi^2_{\text{RM}}$ , and  $\chi^2_{\text{SA}}$  are these that maximize the likelihood ( $\mathcal{L}_{\text{max}}$ ).  $N_{\text{RM}} = 9450$  and  $N_{\text{SA}} = 1000$  are the numbers of RM and SA data points, respectively.

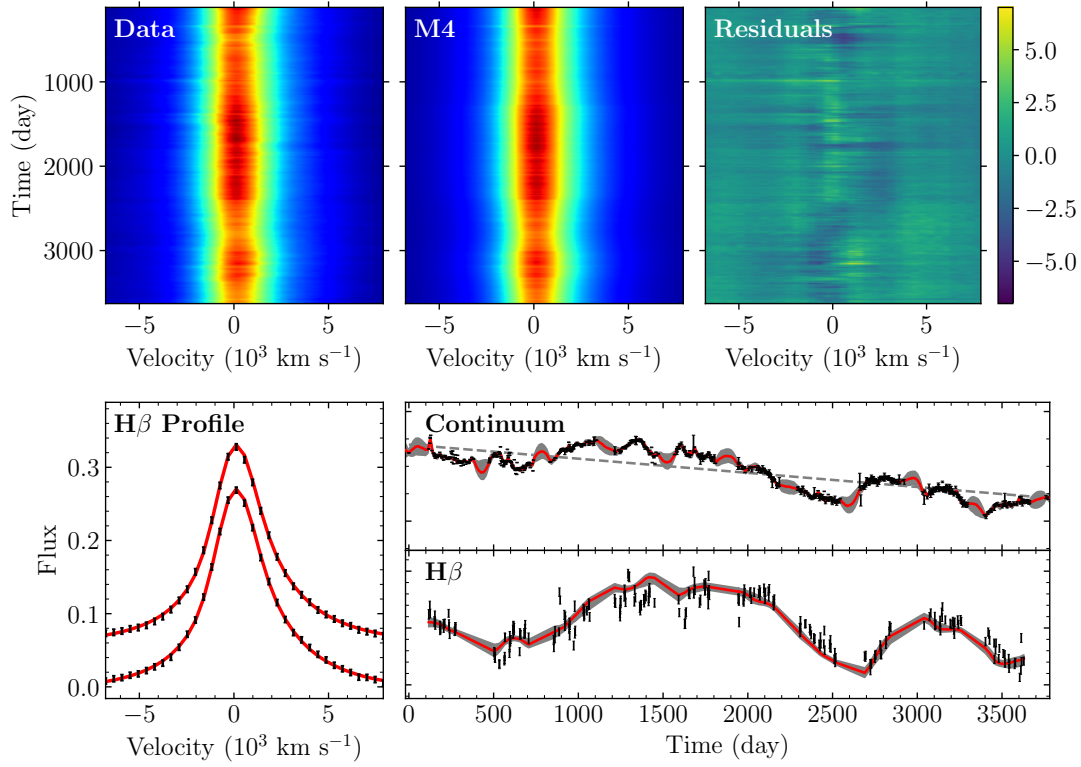


**Figure 5.** Fits to the  $H\beta$  RM data of 3C 273 using model M4. The top three panels show the observed  $H\beta$  spectral time series, a model fit, and the standardized residuals between the observed data and model fit. The bottom left panel shows  $H\beta$  profiles at two selected epochs, superposed upon the model fits with red solid lines. The bottom right panels show the time series of continuum and  $H\beta$  fluxes. The red lines with grey shaded bands represent reconstructions from model fits. Grey dashed line presents the linear polynomial used to detrend the continuum light curve. The observations of continuum light curve are set to start at day zero.

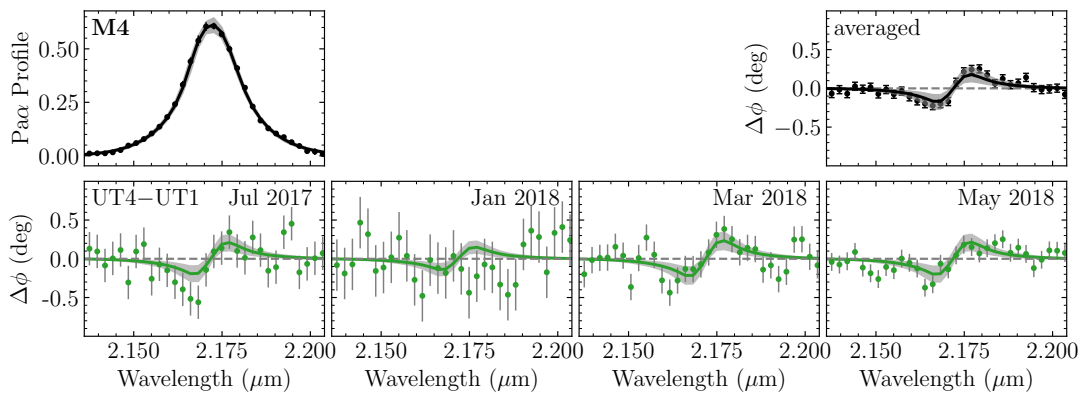


**Figure 6.** Fits to the  $\text{Pa}\alpha$  SA data of 3C 273 using model M4. The top left panel shows the time-averaged  $\text{Pa}\alpha$  profile and the top right panel shows the time-averaged differential phase curves on three of the six baselines (UT4-3, UT4-2, and UT4-1; see also G18). The bottom panels show the differential phase curves on the UT4-1 baseline at four epochs observed by GRAVITY/VLTI (Gravity Collaboration et al. 2018). The solid lines with grey shaded bands show reconstructions from model fits. The wavelengths are given in observed frame. Fits to the full SA data (with six baselines at four epochs) are shown in Appendix. The wavelengths are given in observed frame.

the continuum light curve is detrended by a linear polynomial, indicated by a grey dashed line in the bottom right panel of Figure 5. The radial profile of BLR clouds are described by a double power law (Equation 29) with a slope parameter  $\alpha \sim 1.7$  for the  $H\beta$  BLR and  $\alpha \sim 2.2$  for the  $Pa\alpha$  BLR. In the vertical direction, BLR clouds are more inclined to distribute around the equatorial plane (Equation 33), although the opening angles for both  $H\beta$  and  $Pa\alpha$  BLRs are large.

In Figures 5, we show fits to  $H\beta$  RM data using model M4. The large-scale variation features of the  $H\beta$  spectral time series are generally reproduced, although there are still minor patterns in the residuals. For the integrated  $H\beta$  fluxes in right bottommost panel of Figure 5, our fits again well match the large-scale variations, nevertheless, there appear slight excesses around 1300 days and minor deficits around 2300-2500 days and 3100-3500 days. The reasons for the above minor deviations might be twofold: first, the present simple dynamical BLR models are not expected to reproduce all the fine variation structures; second, for simplicity, we used a linear polynomial to detrend the continuum light curve, which can be only regarded as a zero-order approximation (Li et al. 2020). In Figure 6, we show fits to the  $Pa\alpha$  profile and differential phase curves. For clarity, we only plot the phase curves on one baseline (UT4-UT1) and the time-averaged phase curve on three of the six baselines (UT4-UT3, UT4-UT2, and UT4-UT1; see also G18). Full fits to the phase curves on all six baselines are shown in Appendix. Overall, the  $Pa\alpha$  profile and differential phase curves are also well reproduced, in particular for the baselines UT4-UT3, UT4-UT2, and UT4-UT1 where the phase signals are of high quality.

For the sake of comparison, in Figures 7 and 8, we show fits to the  $H\beta$  RM data and  $Pa\alpha$  SA data using model M8, which has the highest rank among the models (M5-M8) that detrend the continuum light curve with the 15 GHz radio light curve. Again, full fits to the differential phase curves on six baselines with model M8 are shown in Appendix. Similar to model M4, the large-scale  $H\beta$  variation features and  $Pa\alpha$  differential phase curves are overall captured. However, compared to model 4, model 8 additionally yields relatively mild deficits around 3300-3500 days in the  $H\beta$  light curves. The fitting results with the other models are generally similar with M8 and therefore not shown.

Figure 9 compares the posterior values of black hole mass ( $M_\bullet$ ), angular-size distance ( $D_A$ ), inclination angle ( $\theta_{inc}$ ), and position angle (PA) for the 8 models. A remarkable point is that the vertical distribution D $\theta$ 1 systematically yields a larger inclination angle of  $\sim 30^\circ$ , whereas the distribution D $\theta$ 2 yields an inclination angle of  $\sim 6^\circ$ . The latter value is consistent with the inclination  $3.8^\circ$ - $15^\circ$  of the jet in 3C 273 measured by radio observations (e.g., Lobanov & Zensus 2001; Savolainen et al. 2006; Meyer et al. 2016; Jorstad et al. 2017). The main reason for such a dichotomy is as follows (see also discussions in Grier et al. 2017 and Li et al. 2018). In a case of a thin disk-like BLR with clouds preferentially distributed close to the equatorial plane (e.g., D $\theta$ 2), the resulting line profiles are always double-peaked for a large

inclination angle. Therefore, the observed single-peaked profiles of both the  $H\beta$  and  $Pa\alpha$  lines require a small (nearly face on) inclination. By contrast, when BLR clouds preferentially cluster around the outer faces (e.g., D $\theta$ 1), the line profiles tend to be flat in the core as the opening angle increases. Meanwhile, to generate single-peaked profiles, the opening angle should be larger than the inclination angle. As a result, the observed single-peaked profiles require the opening angle to be as small as possible, but still larger than the inclination angle. The final resulting opening angle is approximately equal to the inclination angle, roughly about  $30^\circ$ - $40^\circ$ . Such an approximate equality was commonly seen in previous studies of BLR dynamical modeling (e.g., Pancoast et al. 2014b; Grier et al. 2017; Li et al. 2018; Williams et al. 2018). In this case, the inclination angle cannot be as small as that in the case of D $\theta$ 2 distribution, otherwise the yielded transfer function will be too spiky in wavelength and time-delay space to fit the observations.

The PAs are overall similar, around  $200^\circ$  with a typical uncertainty of  $\sim 20^\circ$ - $30^\circ$ , insensitive to the radial and vertical distributions of BLR clouds. This is because PA is mainly determined by the projected positions of the six baselines on the sky. The PA of the large-scale jet of 3C 273 is about  $222^\circ$  (e.g., Roeser & Meisenheimer 1991), marginally coincident with that of the  $Pa\alpha$  BLR. Figures 9 and 10 also illustrate that the detrending approaches (using a linear polynomial or the radio light curve) have limited influences on the final results.

## 5.2. The Black Hole Mass

We calculate the best estimates and uncertainties of black hole mass and illustrate the posterior distributions in the top panel of Figure 10 for the 8 models. The obtained black hole masses are concentrated around  $10^8 M_\odot$  for cases of vertical distributions D $\theta$ 1 and around  $10^9 M_\odot$  for cases of vertical distributions D $\theta$ 2. Such a large difference is mainly caused by the inclination angles. The LOS velocity is proportional to  $\sin \theta_{inc}$ . Consequently, if regardless of other factors, the black hole mass depend on the inclination as

$$M_\bullet \propto 1/\sin^2 \theta_{inc}. \quad (42)$$

As described above, the obtained inclination for cases of D $\theta$ 1 distribution is about  $30^\circ$  while the inclination for cases of D $\theta$ 2 distribution is about  $6^\circ$ . This can easily lead to a difference in black hole mass by one order of magnitude.

The most probable model M4 yields a black hole mass of  $\log(M_\bullet/M_\odot) = 9.06^{+0.27}_{-0.21}$ . In Figure 11, we show the locations of 3C 273 on the relations between black hole mass and bulge mass and  $K$ -band luminosity compiled by Kormendy & Ho (2013). Figure 11 illustrates that the obtained black hole mass with model M4 is remarkably consistent with the relationships between black hole mass and bulge properties (within  $1.7\sigma$ ), despite a large uncertainty of the bulge mass of 3C 273. This reinforces the model selection based on the Bayes factor. Moreover, the black hole masses of  $\sim 10^8 M_\odot$  obtained by models with the D $\theta$ 1 distribution (M1, M3, M5, and M7) deviate at  $3 - 5\sigma$  confidence levels from the rela-

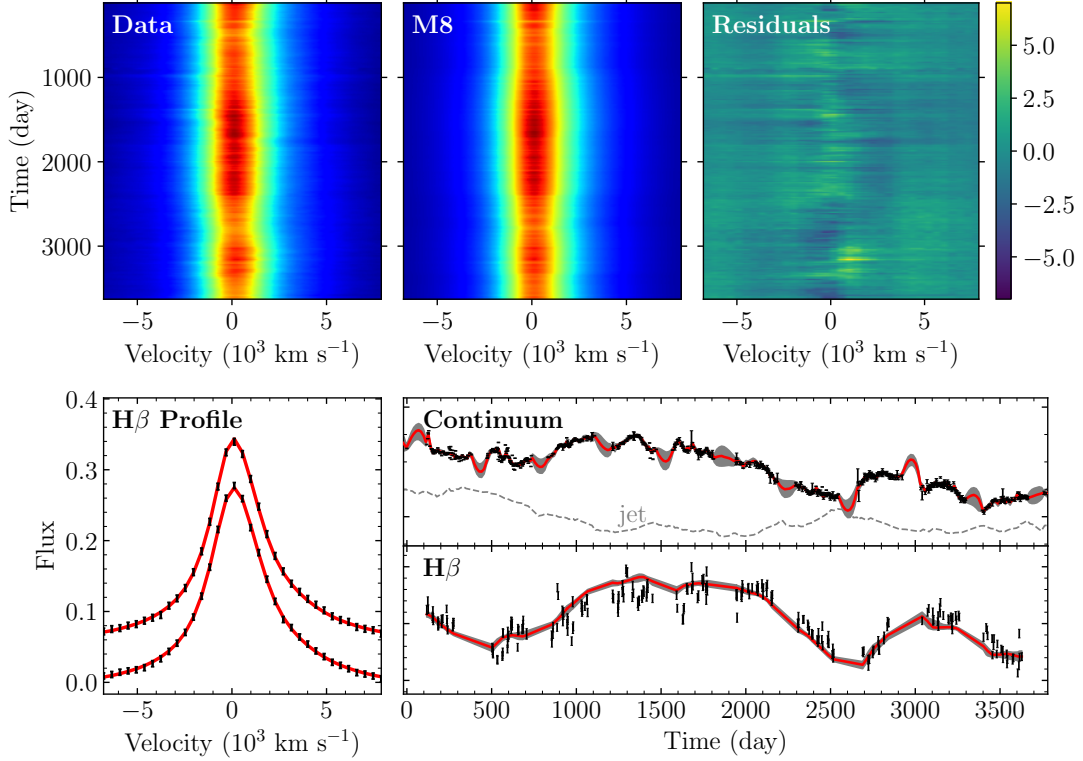


**Figure 7.** Same as Figure 5, but using model M8. Grey dashed line represents the trend subtracted from the continuum light curve, which is derived from the 15 GHz radio light curve with shifting and scaling (see Equation 37).

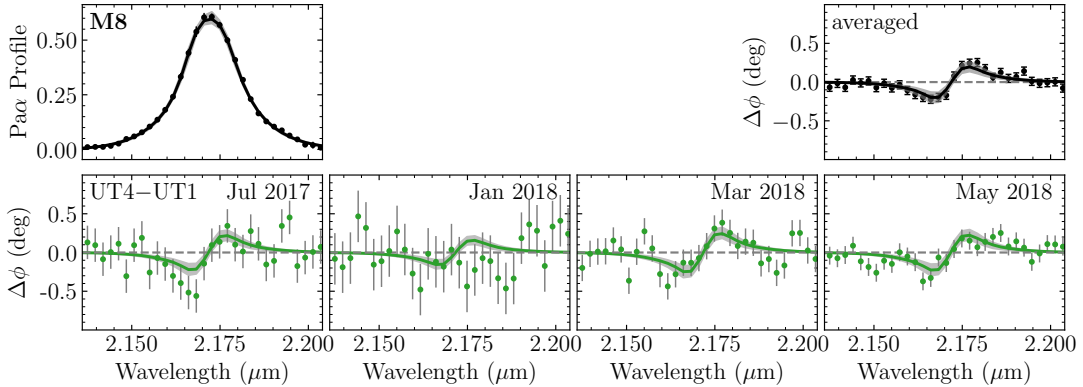


**Figure 8.** Same as Figure 6 but using model M8. Fits to the full SA data (with six baselines at four epochs) are shown in Appendix.

tionships between black hole mass and bulge properties and therefore are statistically not preferable.

### 5.3. The Angular-size Distance

Figures 9 and 10 illustrate that the values of  $D_A$  also depend on vertical distributions of BLR clouds. In models with  $D\theta 2$  distributions (M2/4/6/8), the inferred  $D_A$  is generally larger than that in models with  $D\theta 1$  distributions (M1/3/5/7) by about 0.1-0.5 dex. The  $\Lambda$ CDM cosmology with the latest *Planck* measurements (Planck Collaboration et al. 2020) yields an angular-size distance of  $\log(D_A/\text{Mpc}) = 2.77$  to 3C 273. If we use this value as the fiducial distance, the

models with  $D\theta 2$  distributions yield more reasonable inferences. Among models with the  $D\theta 1$  distribution, M1 and M5 yield results in line with the  $\Lambda$ CDM cosmology within the  $1\sigma$  uncertainty; the distances obtained by M3 and M7 are a bit larger by 0.4 dex, but still consistent with the fiducial value within a  $2.5\sigma$  level. Both models M3 and M7 employ the  $Dr 2$  distribution (double power law) in radial direction and  $D\theta 1$  distribution (concentrated around the equatorial plane) in vertical distribution. The discrepancy possibly implies that a combination of  $Dr 2$  and  $D\theta 1$  might not be preferred.

We stress that the present SARM analysis can naturally obtain the angular-size distance. The above comparison with

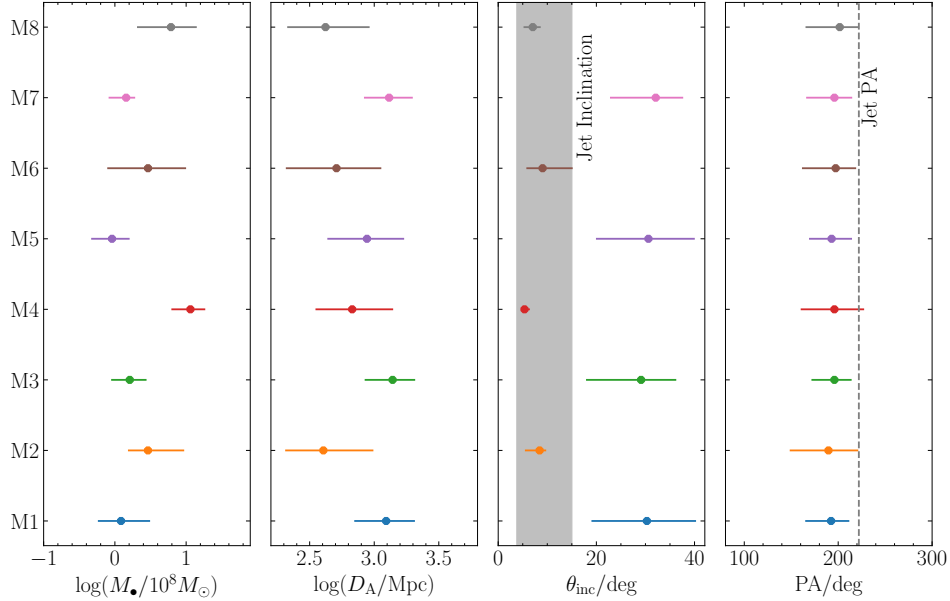


**Figure 9.** Inferred black hole mass, angular-size distance, inclination angle, and position angle for different models. In the third panel, the vertical shaded band represents the inclination angle ( $3.8^\circ$ - $15^\circ$ ) of the jet in 3C 273 from radio measurements. In the rightmost panel, the vertical dashed line represents the position angle of the jet.

the distance from the  $\Lambda$ CDM cosmology is mainly aimed to illustrate the differences among the 8 models.

#### 5.4. Geometry and Kinematics of the $H\beta$ and $\text{Pa}\alpha$ BLRs

In Table 3, we summarize values of the major parameters of all models for both the  $H\beta$  and  $\text{Pa}\alpha$  BLRs. In Figure 12, we compare the posterior distributions of major parameters of the most probable mode M4. For all models (except M2), the obtained  $H\beta$  BLR sizes are generally smaller than the  $\text{Pa}\alpha$  BLR sizes, consistent with the observation that the  $H\beta$  line has a broader width than the  $\text{Pa}\alpha$  line (see Figure 2). In model M2, the  $H\beta$  BLR sizes are comparable to or even larger than the  $\text{Pa}\alpha$  BLR sizes. M2 uses D $\theta$ 2 distribution in the vertical direction (see Table 1). The parameter  $\gamma$  is a bit larger for the  $\text{Pa}\alpha$  line ( $\gamma \sim 3$ ) than that for the  $H\beta$  line ( $\gamma \sim 1.5$ ). Larger  $\gamma$  means that the BLR clouds are more concentrated towards the equatorial plane, giving rise to a larger SA phase amplitude owing to a decrement in the stochastic motion along the LOS. As a result, the  $\text{Pa}\alpha$  BLR size is reduced to match the observed phase amplitudes (Songsheng et al. 2021). However, considering the larger  $\beta$  value of the  $H\beta$  BLR, the resulting clouds are still more compactly distributed than those of the  $\text{Pa}\alpha$  BLR.

Both the  $H\beta$  and  $\text{Pa}\alpha$  BLRs have large opening angles ( $\sim 40^\circ$ - $80^\circ$ ), indicating that they are overall geometrically thick. The values of parameter  $\xi$  for all models are  $\sim 0.4 - 0.8$ , meaning that the equatorial mediums are partially transparent. The values of parameter  $\gamma$  systematically deviate from unity so that the vertical distributions of BLR clouds are neither uniform in light of  $\cos\theta$  nor uniform in light of  $\theta$  (see Section 3.3.1). The parameter  $\kappa$ , used to describe the anisotropy of BLR emissions (Equation 35), has a large posterior range. In models M4 and M8, the posterior distribution

of  $\kappa$  for the  $H\beta$  BLR is double peaked around  $\kappa = -0.5$  and  $0.3$  (e.g., see Figure 12). Overall,  $\gamma$  is not well constrained under present data quality.

In Figure 13, for the sake of comparison, we show examples of cloud distributions of the  $H\beta$  and  $\text{Pa}\alpha$  BLRs for models M1-M4. We can clearly find that the  $H\beta$  BLR is more compact than the  $\text{Pa}\alpha$  BLR. A recent photoionization calculation by Zhang et al. (2021) showed that the emissivity of the  $H\beta$  line decreases with radius more rapidly than that of the  $\text{Pa}\alpha$  line. This indicates that the difference between the two BLRs arises from the intrinsic photoionization process.

Regarding dynamics, there is a fair fraction ( $1 - f_{\text{ellip}}$ ) of BLR clouds in inflowing/outflowing motion. The parameter  $f_{\text{flow}}$  is also not well constrained and has a large uncertainty for all models. Figure 12 demonstrates that for the  $H\beta$  BLR in model M4,  $f_{\text{flow}}$  tends to be  $< 0.5$ , which means that inflowing clouds are relatively preferred. This is consistent with the velocity-binned delay map obtained by Zhang et al. (2019), which showed a longer time delay in blue velocity bins, a signature believed to indicate inflows (Peterson 2014).

## 6. DISCUSSIONS

### 6.1. Compared to the SA Modeling of G18

G18 applied a simple dynamical model to interpret the SA data of 3C 273. In their model, BLR clouds follow a gamma distribution (Dr1) in radial direction and a uniform distribution in vertical direction (D $\theta$ 2 with  $\gamma = 1$ ). Such a geometry is somehow similar to that of model M2 and M6 if fixing  $\gamma = 1$ . However, for dynamics, G18 assumed circular Keplerian motion and did not include elliptical orbits and inflows/outflows. To determine the black

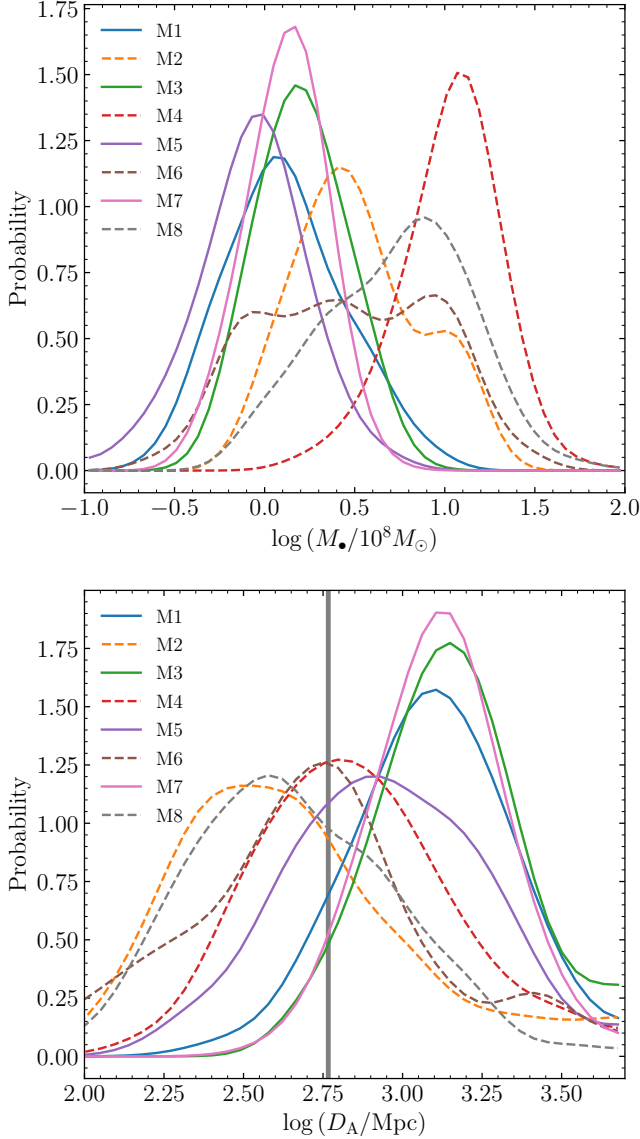


**Figure 10.** Posterior distributions of black hole mass and angular-size distance. Solid and dashed colored lines correspond to BLR models with the D01 and D02 distribution, respectively. In the bottom panel, the vertical grey line represents an angular-size distance of  $D_A = 585$  Mpc.

hole mass from only SA data, G18 preassigned a value of  $\log(D_A/\text{Mpc}) = 2.74$  for the angular-size distance of 3C 273, roughly coincident with the inferred value of  $2.61^{+0.39}_{-0.30}$  by model M2 and  $2.71^{+0.39}_{-0.35}$  by model M6. G18<sup>6</sup> obtained a Pa $\alpha$  BLR size of  $\log(R_{\text{BLR}}/\text{lt-day}) = 2.16^{+0.05}_{-0.06}$  and a black hole mass of  $\log(M_\bullet/10^8 M_\odot) = 0.41^{+0.10}_{-0.13}$ . By a comparison, with model M2, our determined BLR

size  $\log(R_{\text{BLR}}/\text{lt-day}) = 2.07^{+0.22}_{-0.11}$  and black hole mass  $\log(M_\bullet/10^8 M_\odot) = 0.46^{+0.51}_{-0.28}$  (see Table 3). With model M6, the corresponding values are  $\log(R_{\text{BLR}}/\text{lt-day}) = 1.90^{+0.34}_{-0.22}$  and  $\log(M_\bullet/10^8 M_\odot) = 0.46^{+0.53}_{-0.57}$ . These quantities are consistent with the inferences of G18 within uncertainties. Nevertheless, the much smaller uncertainties in G18 may be ascribed to the fixed angular-size distance  $D_A$  and a simple BLR dynamical model.

We note that our obtained inclination angle  $\theta_{\text{inc}} = 8^{+1}_{-3}$  degrees by model M2 and  $9^{+6}_{-3}$  degrees, slightly smaller than the G18 value of  $12 \pm 2$  degrees. This might be the main reason responsible for slightly larger black hole masses in our analysis.

### 6.2. Compared to the 1D SARM Analysis of W20

As described above, W20 conducted the first SARM analysis on the SA and 1D RM data of 3C 273 following the same simple dynamical model in G18. Because only using 1D RM data, W20 assumed that the H $\beta$  and Pa $\alpha$  lines stem from exactly the same BLR and neglected the differences between the two lines by a zero-order approximation. We relax this restrict of a common BLR for the H $\beta$  and Pa $\alpha$  by treating the two BLRs separately and let them only share the black hole mass and inclination. To this end, 2D RM data are required. Such 2D SARM analysis is more generally applicable, particularly in cases where SA and RM data are observed in different periods.

W20 obtained a black hole mass of  $\log(M_\bullet/10^8 M_\odot) = 0.75^{+0.07}_{-0.07}$ , angular-size distance of  $\log(D_A/\text{Mpc}) = 2.74^{+0.07}_{-0.07}$ , and inclination of  $\theta_{\text{inc}} = 8.4^{+1.0}_{-0.9}$  degrees. The distance is consistent within uncertainties with our obtained value by the most probable model M4 (see Table 3), however, the black hole mass is slightly lower than our inference. Again, this is because of a mildly larger inclination of W20 than ours (see Equation 42). We note that W20 reported significantly smaller uncertainties of model parameters than ours. The reasons are might be twofold. First, the assumption that the H $\beta$  and Pa $\alpha$  BLRs are identical leads to more strict constraints on model parameters. Second, compared to W20, we adopted a more generous BLR model that includes additional ingredients such as anisotropy of BLR emissions, transparency of the equatorial plane, elliptical orbits and inflow/outflows. These ingredients are necessary because the H $\beta$  profile are slightly asymmetric and the velocity-resolved delay map of the H $\beta$  line shows complicated structures (Zhang et al. 2019), which are unlikely to be reproduced with the simple BLR model in G18.

### 6.3. Model Dependence

Our results illustrate that the obtained BLR parameters (such as black hole mass and angular-size distance) are insensitive to specific geometric configurations and continuum detrending schemes, but more or less depend on parameterizations of the vertical distributions. As mentioned in Section 5.1, the vertical distribution D01 (in which clouds tend to cluster close to the outer BLR faces) yields an inclination angle of  $\theta_{\text{inc}} \sim 30^\circ$  and black hole mass of  $M_\bullet \sim 10^8 M_\odot$ . By

<sup>6</sup> Note that the uncertainties in G18 were quoted with 90% ( $1.65\sigma$ ) confidence intervals. Here we simply divide the uncertainties by a factor of 1.65 to be consistent with  $1\sigma$  confidence intervals used in this work.

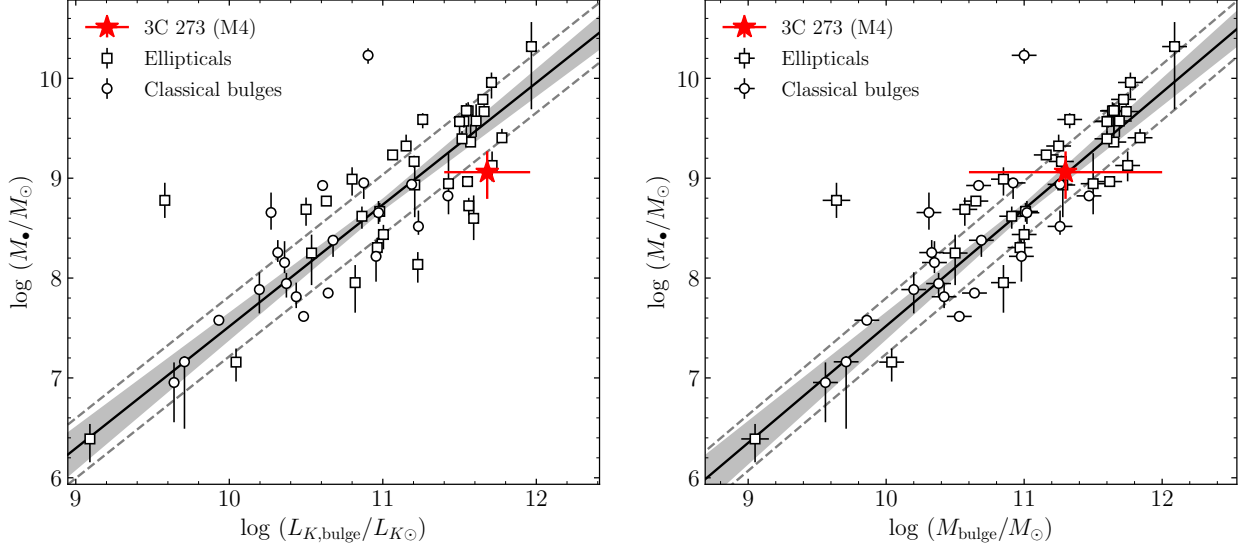


**Figure 11.** The relations between black hole mass and (left)  $K$ -band bulge luminosity and (right) bulge mass of classical bulges and ellipticals compiled by Kormendy & Ho (2013). Solid lines with shaded areas represent the linear regression fits from Kormendy & Ho (2013). Grey dashed lines represent the intrinsic scatters of the relations. Superimposed is 3C 273 (red star) with the mass obtained using model M4 and the bulge mass and luminosity derived from Zhang et al. (2019) using the *Hubble Space Telescope*/WFC3 images.

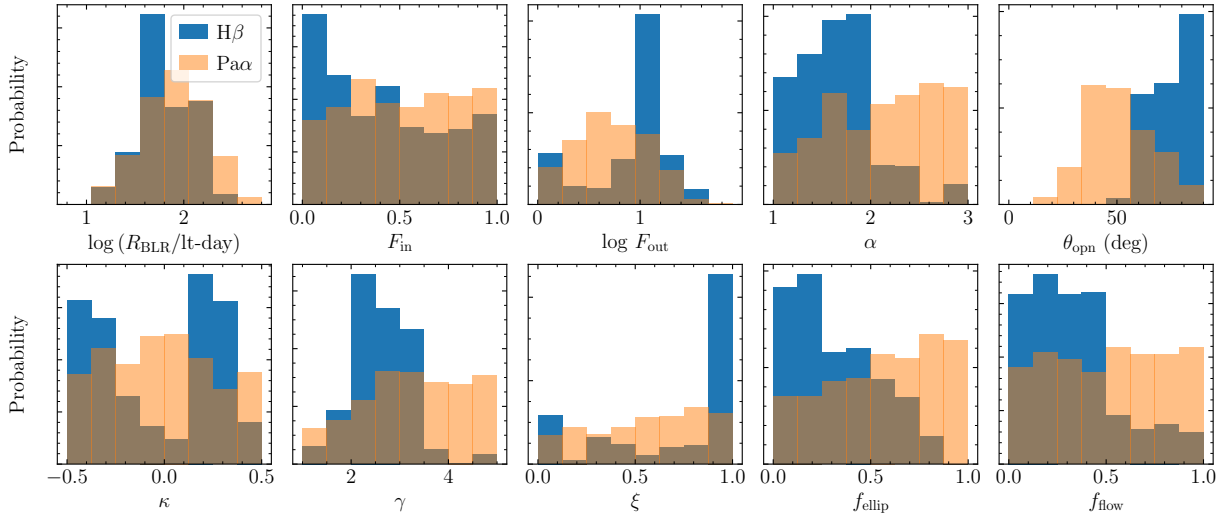


**Figure 12.** The posterior distributions of major parameters of the most probable model M4 for the  $H\beta$  and  $Pa\alpha$  BLRs (see Section 4.1 for the sampling coverage checking in diffusive nested sampling).

contrast, the distribution  $D\theta 2$  systematically yields a smaller inclination angle of  $\theta_{inc} \sim 6^\circ$  and higher black hole mass of  $M_\bullet \sim 10^9 M_\odot$ .

As described in the preceding sections, the statistic tests with the Bayes factor and maximum likelihood also rank M4 as the most probable model. The inclination angle and black hole mass obtained by M4 are all consistent with other independent constraints. This implies that it is possible to employ Bayesian statistics to select out the most probable model in cases without independent information. The Monte Carlo tests performed by Gravity Collaboration et al. (2020a) also confirmed the feasibility of using Bayesian statistics. More

cases of SARM analysis with independent observational constraints like 3C 273 presented in this work would testify the use of Bayesian model selection.

In addition, for AGNs with broad emission lines, polarized spectra are expected to arise from the scattering electrons in the equatorial plane, which is effectively equivalent to an edge-on viewer (e.g., Smith et al. 2002; Afanasiev & Popović 2015; Songsheng & Wang 2018). It is thus possible that spectropolarimetry of broad emission lines may provide independent information of the vertical distributions of BLRs, which is helpful to testify the results in the present

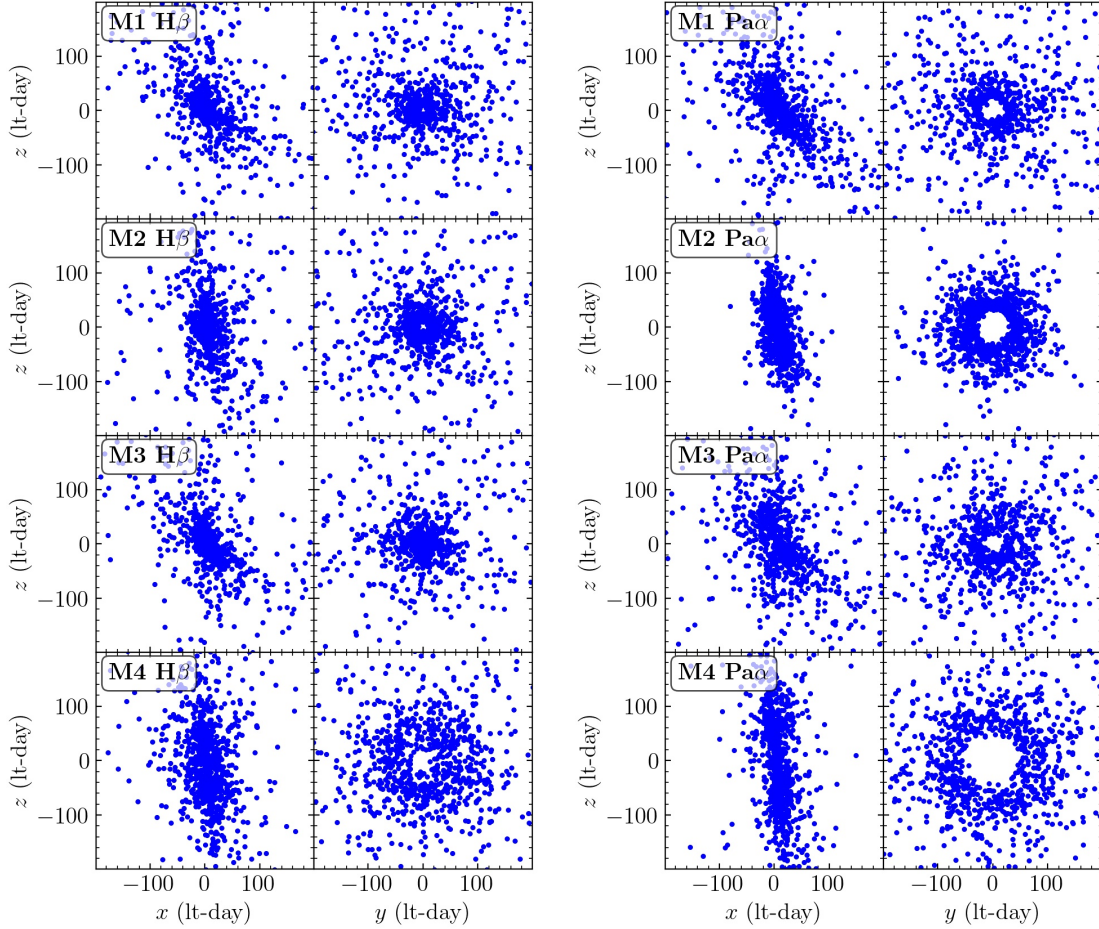


**Figure 13.** Examples of cloud distributions of the  $H\beta$  and  $Pa\alpha$  BLRs for models M1-M4 using the best parameter values listed in Table 3. The LOS is along the positive  $x$ -axis.

SARM analysis. In this sense, spectropolarimetric observations merit investigations in future.

#### 6.4. Parameter Sharing of the $H\beta$ and $Pa\alpha$ BLRs

In consideration of the different  $H\beta$  and  $Pa\alpha$  line shapes (see Figure 2), we relax the restrict that the two lines have a common BLR and treat their respective BLRs separately. We let the two BLRs share the black hole mass and inclination angle. This is the most conservative and unbiased implementation in so far as it is not yet clear which factors are responsible for the noticeable differences in the two lines. However, it is clear that any inappropriate parameter sharing of the two BLRs will cause biased results. The disadvantage of our present scheme of parameter sharing is that the obtained parameter uncertainties are relatively large, compared to full parameter sharing (see Section 6.2). This disadvantage can be compensated by higher-quality RM data so that the black hole mass can be constrained more precisely. Moreover, future better understanding of BLR geometry and kinematics by including photoionization modeling may be beneficial to revealing the reasons for the different line shapes, therefore shedding light onto the parameter sharing.

#### 6.5. Joint Bayesian Analysis

In Table 3, we list  $\chi^2$  of the best fits for the SA and RM data separately. Because of much larger number of points in the RM data, the  $\chi^2$  value is dominated by RM fitting, which thus far out weights SA fitting in present recipe of joint analysis. Meanwhile, the computational time for calculating  $H\beta$  profile series is much intensive than that for calculating  $Pa\alpha$  profile and differential phase curves. A possible procedure surmounting these issues is using the posterior from the SA fitting as the prior for the RM fitting (e.g., see Alsing & Handley 2021). In generic, the posteriors might be complicated than single Gaussians. There is an increasingly popular technique, called normalizing flows, that provides a general framework to transform any forms of posteriors to expressive probability distributions easy to deal with in MCMC sampling (see a review of Papamakarios et al. 2021). It is worth incorporating this technique to our SARM analysis in future so as to expedite MCMC sampling.

#### 6.6. Possible Systematics and Future Improvements

There are two remarks meriting further discussions in our calculations.

First, we assume that BLR clouds rotate coherently in a way that each cloud’s angular momentum is diverse but overall has a component oriented toward a common rotation axis. SA signals sensitively depend on the degree of coherent motion of BLR clouds (e.g., Songsheng et al. 2019). This is because at a given velocity bin, the summation of the angular displacements will be canceled out once displacements are in mutually opposite directions (see Equation 10). In an extreme case, orbital motion of BLR clouds with fully random angular momentum would not produce SA signals. The degree of coherent motion depends on specific formation scenarios of BLRs (e.g., Baskin et al. 2014; Wang et al. 2017; Czerny et al. 2017). Other independent measurements about BLRs (such as spectropolarimetry) may be beneficial to justify the BLR scenarios and determine the degree of coherent motion.

Second, we include nonlinear responses of clouds’ emissions to the incident continuum, described by a parameter  $\delta$ . The conventional quantity, responsivity of clouds’ emissions  $\eta$ , is related to the nonlinear parameter as  $\eta = 1 + \delta$  (see Section 3.1). For simplicity, we assumed that  $\delta$  and thereby  $\eta$  are constant temporally and spatially so that the resulting emissivity-weighted and responsivity-weighted transfer functions are identical (see Section 3.2). In reality, photoionization calculations shows that the responsivity depends on local gas properties (such as density and ionizing photon flux) and therefore may deviate from a constant (e.g., Korista & Goad 2004; Goad & Korista 2014; Zhang et al. 2021). A future improvement by incorporating photoionization processes will help to address this issue. On the other hand, the usual dispute that RM measures responsivity-weighted parts while SA measures emissivity-weighted parts of BLRs can be inherently resolved in present 2D SARM analysis. This is because we treat separately the BLRs for RM data and SA data. The connections between the two BLRs are the mutual SMBH mass and view inclination, rather than the mutual BLR size. Remarkably, such SARM analysis does not require SA and RM observations to undertake in the same periods and is also not affected by AGN intrinsic variability. However, as mentioned in Section 6.4, this approach leads to a longer list of model parameters and thus larger uncertainties in parameter inferences. On the theoretical side, better understandings of BLR dynamics and emission processes for different broad emission lines are required; on the observational side, high-fidelity data (namely, with high signal to noise ratios and high and homogeneous cadences) are important to make improved measurements on black hole masses and distances.

### 6.7. Measurement Uncertainties

Our obtained SMBH mass has an uncertainty of about 0.24 dex, which translates to a large uncertainty of the angular-size distance (because the SA and RM data sets are linked through black hole mass and inclination). As mentioned in Section 6.5, the  $\chi^2$  value of the joint analysis is dominated by the RM data. For the sake of comparison, in Figure 14, we compile the reported uncertainties of SMBH mass infer-

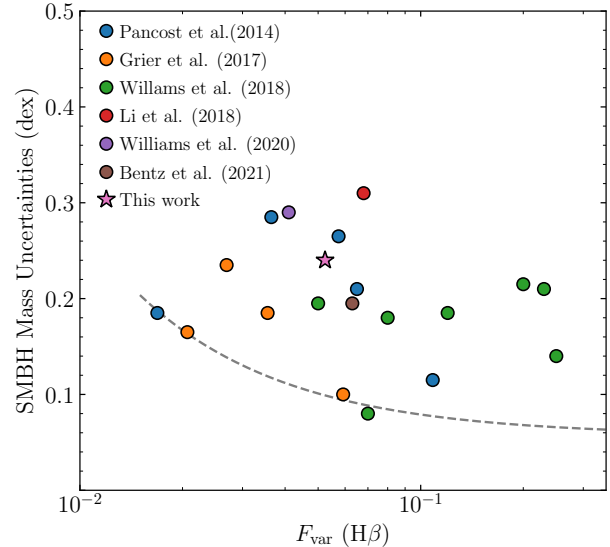


**Figure 14.** The reported uncertainties of SMBH masses with fractional variability  $F_{\text{var}}$  of the  $H\beta$  light curves from previous BLR dynamical modeling (see the text). The asterisk point represents 3C 273 in this work. The dashed line represents a simple extrapolation of minimum achievable uncertainties to large variability.

ences with fractional variability of the  $H\beta$  light curves from previous BLR dynamical modeling with RM data (Pancost et al. 2014b; Gravity Collaboration et al. 2017; Williams et al. 2018, 2020; Li et al. 2018). Here, fractional variability measures the excess variance of a light curve, defined as  $F_{\text{var}} = \sqrt{\delta^2 - \sigma^2} / \langle F \rangle$ , where  $\delta^2$  is the variance of the fluxes,  $\sigma^2$  is the mean square uncertainty, and  $\langle F \rangle$  is the mean flux (Rodríguez-Pascual et al. 1997). If regardless of other influence factors (such as cadences and time spans), a large  $F_{\text{var}}$  means that there are more significant variances in the light curves, which facilitates reverberation analysis and thereby leads to stronger constraints on parameter inferences. To guide eye, we use a line to extrapolate minimum achievable uncertainties to large variability in Figure 14. With adequate variability and data quality, it seems possible to achieve a statistical uncertainty of SMBH mass down to  $<0.1$  dex (e.g., see Williams et al. 2021). For our present SARM analysis approach, a high-precision SMBH mass determination from the RM fitting effectively puts a strong prior to the SA fitting, therefore beneficial to yielding a competitive measurement on the angular-size distance.

## 7. CONCLUSIONS

We construct a suite of BLR dynamical models with different geometric configurations and conduct joint SARM analysis on the Pa $\alpha$  SA data and 2D  $H\beta$  RM data of 3C 273. We consider two types of radial distributions and two types of vertical distributions. In addition, a detrending procedure is needed to subtract the long-term trend in the continuum light curve (Zhang et al. 2019), which can be explained by the jet contaminations (Li et al. 2020). We use either a lin-

ear polynomial or the radio light curve of 3C 273 for the detrending procedure. We finally have 8 BLR models with different combinations of the above ingredients. On account of different  $H\beta$  and  $\text{Pa}\alpha$  line profiles, we treat their BLRs separately but let them only share the inclination angle and SMBH mass. This allows us to determine the mass and angular-size distance of the SMBH in 3C 273 simultaneously in a self-consistent way. Such a treatment has general applicability in cases where SA and RM observations are undertaken in different periods.

We develop a Bayesian framework and employ a Markov-chain Monte Carlo technique with the diffusive nested sampling algorithm (Brewer et al. 2011) to explore the posterior probabilities of the BLR dynamical models. Across the 8 models, the most probable model with the maximum likelihood and Bayes factor is the one (M4 in Table 1) in which the radial distribution of BLR clouds is double power laws and the vertical distribution tends to concentrate around the equatorial plane. The obtained inclination angle is  $5_{-1}^{+1}$  deg, coincident with the inclination of the large-scale jet in 3C 273 (see Section 4.2). The best determined angular-size distance is  $\log(D_A/\text{Mpc}) = 2.83_{-0.28}^{+0.32}$ , and black hole mass is  $\log(M_\bullet/M_\odot) = 9.06_{-0.27}^{+0.21}$ , which agrees with the relationships between black hole mass and bulge properties (see Figure 11). Both the  $H\beta$  and  $\text{Pa}\alpha$  BLRs are geometrically thick and consist of a fraction of bound elliptical motion. The rest fraction are inflows or outflows, which cannot be distinguished with the present data, although inflows in the  $H\beta$  BLRs are more preferable.

The final results are insensitive to the radial distribution of BLR clouds and the detrending approaches of the continuum light curve. Nevertheless, we find that the obtained black hole mass and angular-size distance depend more or less on the vertical distribution of BLR clouds. Specifically, the distribution ( $D\theta 1$  in Section 3.3.1) with BLR clouds clustering around the outer BLR faces results in a larger inclination angle and smaller black hole mass, just contrary to the distribution ( $D\theta 2$  in Section 3.3.1) with BLR clouds concentrated towards the equatorial plane. By comparing with other independent information about the inclination angle from the radio observations and the black hole mass from the relationships between black hole mass and bulge properties, our

results implies that it is possible to use Bayesian statistics to determine the preferred model.

With the present data quality of 3C 273, the obtained black hole mass, angular-size distance, and other parameters have relatively large uncertainties. Future high-fidelity SA and RM data (e.g., high signal to noise ratios and high and homogeneous cadences) may help to determine the BLR geometry and kinematics, black hole mass, and angular-size distance more precisely. Meanwhile, alternative independent measurements on black hole mass such as through stellar/gas dynamics (e.g., Kormendy & Ho 2013; Barth et al. 2016; Bentz 2016) or through spectropolarimetry (e.g., Afanasiev & Popović 2015; Songsheng & Wang 2018) may also be valuable for this purpose.

#### ACKNOWLEDGMENTS

We thank the referee for useful suggestions that improve the manuscript and the GRAVITY Collaboration for useful discussions and kindly sharing the GRAVITY observation data of 3C 273 through E. Sturm. We also thank Yulin Zhao for deriving the  $K$ -band bulge luminosity of 3C 273. This work is supported by the National Key R&D Program of China through grant No. 2016YFA0400701, by the National Science Foundation of China (NSFC) through grant No. 11833008, 11991051, and 11991054, by the China Manned Space Project through No. CMS-CSST-2021-A06 and CMS-CSST-2021-B11, and by the CAS International Partnership Program (113111KYSB20200014). Y.R.L. acknowledges financial support from NSFC through grant No. 11922304 and from the Youth Innovation Promotion Association CAS. P.D. acknowledges financial support from NSFC through grant No. 12022301 and 11873048. C.H. acknowledges financial support from NSFC through grant No. 11773029. M.X. acknowledges financial support from NSFC through grant No. 12003036.

This research has made use of data from the Steward Observatory spectropolarimetric monitoring project, which is supported by Fermi Guest Investigator grants NNX08AW56G, NNX09AU10G, NNX12AO93G, and NNX15AU81G. This research has also made use of data from the OVRO 40 m monitoring program, which is supported in part by NASA grants NNX08AW31G, NNX11A043G, and NNX14AQ89G and NSF grants AST-0808050 and AST-1109911.

*Software:* CDNest (Li 2020), DASpec (<https://github.com/PuDu-Astro/DASpec>), BRAINS (Li et al. 2018)

#### APPENDIX

This appendix shows the full fits to the SA data of 3C 273 using models M4 and M8 in Figures 15 and 16.

#### REFERENCES

- Afanasiev, V. L. & Popović, L. Č. 2015, *ApJL*, 800, L35.  
<https://doi.org/10.1088/2041-8205/800/2/L35>
- Alsing, J. & Handley, W. 2021, *MNRAS*, 505, L95.  
<https://doi.org/10.1093/mnras/slab057>

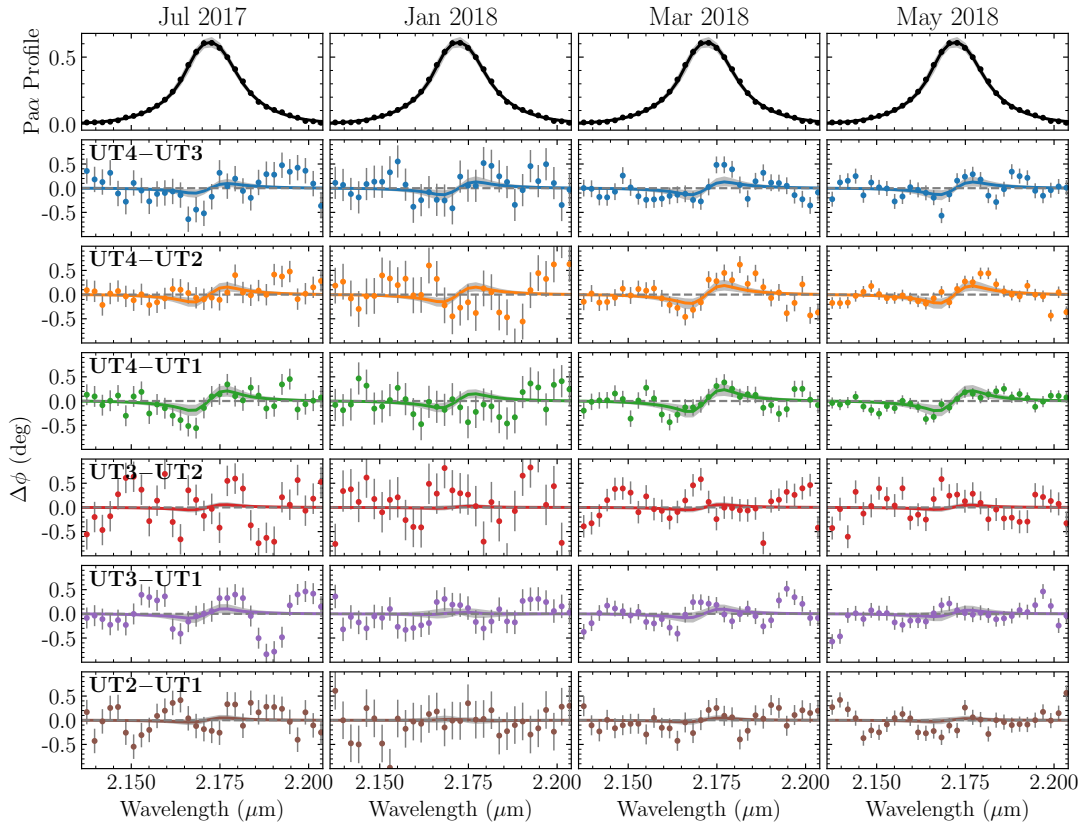


**Figure 15.** Fits to the  $\text{Pa}\alpha$  SA data of 3C 273 using model M4. The topmost four panels show the time-averaged  $\text{Pa}\alpha$  profile (identical in each panel). The rest panels show the differential phase curves on the six baselines (rows) at four epochs (columns) observed by GRAVITY/VLTI (Gravity Collaboration et al. 2018). The solid lines with grey shaded bands show reconstructions from model fits. The wavelengths are given in observed frame.

Bahcall, J. N. & Hills, R. E. 1973, *ApJ*, 179, 699.

<https://doi.org/10.1086/151909>

Bahcall, J. N., Kozlovsky, B.-Z., & Salpeter, E. E. 1972, *ApJ*, 171, 467. <https://doi.org/10.1086/151300>

Baldwin, J. A. 1977, *ApJ*, 214, 679. <https://doi.org/10.1086/155294>

Barth, A. J., Boizelle, B. D., Darling, J., et al. 2016, *ApJL*, 822, L28. <https://doi.org/10.3847/2041-8205/822/2/L28>

Barth, A. J., Pancoast, A., Bennert, V. N., et al. 2013, *ApJ*, 769, 128. <https://doi.org/10.1088/0004-637X/769/2/128>

Bailey, J. A. 1998, *Proc. SPIE*, 3355, 932.

<https://doi.org/10.1117/12.316802>

Baskin, A., Laor, A., & Stern, J. 2014, *MNRAS*, 438, 604.

<https://doi.org/10.1093/mnras/stt2230>

Beckers, J. M. 1982, *Optica Acta*, 29, 361.

<https://doi.org/10.1080/713820871>

Bentz, M. C. 2016, *Astronomy at High Angular Resolution*, 249.

[https://doi.org/10.1007/978-3-319-39739-9\\_13](https://doi.org/10.1007/978-3-319-39739-9_13)

Bentz, M. C., Denney, K. D., Grier, C. J., et al. 2013, *ApJ*, 767,

149. <https://doi.org/10.1088/0004-637X/767/2/149>

Blandford, R. D. & McKee, C. F. 1982, *ApJ*, 255, 419.

<https://doi.org/10.1086/159843>

Bonning, E., Urry, C. M., Bailyn, C., et al. 2012, *ApJ*, 756, 13.

<https://doi.org/10.1088/0004-637X/756/1/13>

Boroson, T. A. & Green, R. F. 1992, *ApJS*, 80, 109.

<https://doi.org/10.1086/191661>

Bosco, F., Hennawi, J. F., Stern, J. et al. 2021, *ApJ* in press (arXiv: 2106.15900)

Brewer, B., & Foreman-Mackey, D. 2018, *Journal of Statistical*

*Software*, 86, 1. <https://doi.org/10.18637/jss.v086.i07>

Brewer, B. J., Páatay, L. B., & Csányi, G. 2011, *Stat. Comput.*, 21,

649. <https://doi.org/10.1007/s11222-010-9198-8>

Burbidge, E. M., Burbidge, G. R., & Prendergast, K. H. 1963, *ApJ*, 137, 1022. <https://doi.org/10.1086/147580>

Cackett, E. M. & Horne, K. 2006, *MNRAS*, 365, 1180.

<https://doi.org/10.1111/j.1365-2966.2005.09795.x>

Courvoisier, T. J.-L. 1998, *A&A Rv*, 9, 1.

<https://doi.org/10.1007/s001590050013>

Czerny, B., Li, Y.-R., Hryniewicz, K., et al. 2017, *ApJ*, 846, 154.

<https://doi.org/10.3847/1538-4357/aa8810>

Denney, K. D., Peterson, B. M., Pogge, R. W., et al. 2010, *ApJ*,

721, 715. <https://doi.org/10.1088/0004-637X/721/1/715>

De Rosa, G., Fausnaugh, M. M., Grier, C. J., et al. 2018, *ApJ*, 866,

133. <https://doi.org/10.3847/1538-4357/aadd11>

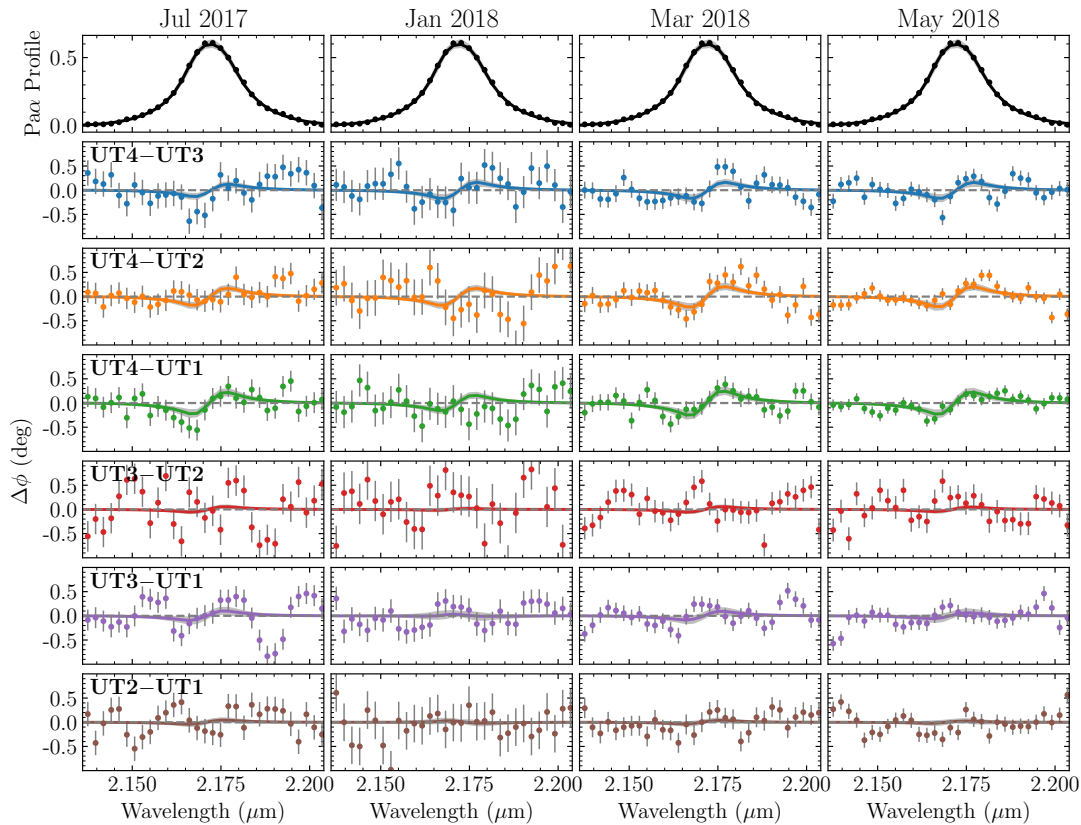


**Figure 16.** Same as Figure 15, but using model M8.

- Du, P., Brotherton, M. S., Wang, K., et al. 2018, *ApJ*, 869, 142.  
<https://doi.org/10.3847/1538-4357/aaed2c>
- Du, P., Hu, C., Lu, K.-X., et al. 2014, *ApJ*, 782, 45.  
<https://doi.org/10.1088/0004-637X/782/1/45>
- Du, P., Lu, K.-X., Hu, C., et al. 2016, *ApJ*, 820, 27.  
<https://doi.org/10.3847/0004-637X/820/1/27>
- Du, P. & Wang, J.-M. 2019, *ApJ*, 886, 42.  
<https://doi.org/10.3847/1538-4357/ab4908>
- Durré, M. & Mould, J. 2021, arXiv:2110.03890
- Elvis, M. & Karovska, M. 2002, *ApJL*, 581, L67.  
<https://doi.org/10.1086/346015>
- Fausnaugh, M. M., Grier, C. J., Bentz, M. C., et al. 2017, *ApJ*, 840, 97. <https://doi.org/10.3847/1538-4357/aa6d52>
- Fitzpatrick, E. L. 1999, *PASP*, 111, 63.  
<https://doi.org/10.1086/316293>
- Goad, M. R. & Korista, K. T. 2014, *MNRAS*, 444, 43.  
<https://doi.org/10.1093/mnras/stu1456>
- Goad, M. R., O'Brien, P. T., & Gondhalekar, P. M. 1993, *MNRAS*, 263, 149. <https://doi.org/10.1093/mnras/263.1.149>
- Gravity Collaboration, Abuter, R., Accardo, M., et al. 2017, *A&A*, 602, A94. <https://doi.org/10.1051/0004-6361/201730838>
- Gravity Collaboration, Amorim, A., Bauböck, M., et al. 2020a, *A&A*, 643, A154.  
<https://doi.org/10.1051/0004-6361/202039067>
- Gravity Collaboration, Amorim, A., Bauböck, M., et al. 2021a, *A&A*, 648, A117.  
<https://doi.org/10.1051/0004-6361/202040061>
- Gravity Collaboration, Amorim, A., Bauböck, M., et al. 2021b, *A&A*, 654, A85. <https://doi.org/10.1051/0004-6361/202141426>
- Gravity Collaboration, Dexter, J., Shangguan, J., et al. 2020b, *A&A*, 635, A92. <https://doi.org/10.1051/0004-6361/201936767>
- Gravity Collaboration, Sturm, E., Dexter, J., et al. 2018, *Nature*, 563, 657. <https://doi.org/10.1038/s41586-018-0731-9>
- Gregory, P. C. 2011, *MNRAS*, 410, 94.  
<https://doi.org/10.1111/j.1365-2966.2010.17428.x>
- Grier, C. J., Pancoast, A., Barth, A. J., et al. 2017, *ApJ*, 849, 146.  
<https://doi.org/10.3847/1538-4357/aa901b>
- Grier, C. J., Peterson, B. M., Horne, K., et al. 2013, *ApJ*, 764, 47.  
<https://doi.org/10.1088/0004-637X/764/1/47>
- Hoyle, F. & Burbidge, G. R. 1966, *ApJ*, 144, 534.  
<https://doi.org/10.1086/148635>
- Hu, C., Wang, J.-M., Ho, L. C., et al. 2012, *ApJ*, 760, 126.  
<https://doi.org/10.1088/0004-637X/760/2/126>
- Hönig, S. F., Watson, D., Kishimoto, M., et al. 2014, *Nature*, 515, 528. <https://doi.org/10.1038/nature13914>
- Jeffreys, H. 2003, *Theory of Probability*, 3rd ed. (Oxford: Clarendon Press), p. 432

- Jorstad, S. G., Marscher, A. P., Morozova, D. A., et al. 2017, *ApJ*, 846, 98. <https://doi.org/10.3847/1538-4357/aa8407>
- Kaspi, S., Smith, P. S., Netzer, H., et al. 2000, *ApJ*, 533, 631. <https://doi.org/10.1086/308704>
- Kim, D., Im, M., & Kim, M. 2010, *ApJ*, 724, 386. <https://doi.org/10.1088/0004-637X/724/1/386>
- Kochanek, C. S., Shappee, B. J., Stanek, K. Z., et al. 2017, *PASP*, 129, 104502. <https://doi.org/10.1088/1538-3873/aa80d9>
- Korista, K. T. & Goad, M. R. 2004, *ApJ*, 606, 749. <https://doi.org/10.1086/383193>
- Kormendy, J. & Ho, L. C. 2013, *ARA&A*, 51, 511. <https://doi.org/10.1146/annurev-astro-082708-101811>
- La Franca, F., Bianchi, S., Ponti, G., et al. 2014, *ApJL*, 787, L12. <https://doi.org/10.1088/2041-8205/787/1/L12>
- Landt, H., Bentz, M. C., Ward, M. J., et al. 2008, *ApJS*, 174, 282. <https://doi.org/10.1086/522373>
- Li, Y.-R. 2020, CDNest: A diffusive nested sampling code in C, v0.2.0, Zenodo, <https://doi.org/10.5281/zenodo.3884449>
- Li, Y.-R., Songsheng, Y.-Y., Qiu, J., et al. 2018, *ApJ*, 869, 137. <https://doi.org/10.3847/1538-4357/aace6b>
- Li, Y.-R., Wang, J.-M., Ho, L. C., Du, P., & Bai, J.-M. 2013, *ApJ*, 779, 110. <https://doi.org/10.1088/0004-637X/779/2/110>
- Li, Y.-R., Zhang, Z.-X., Jin, C., et al. 2020, *ApJ*, 897, 18. <https://doi.org/10.3847/1538-4357/ab95a3>
- Lu, K.-X., Du, P., Hu, C., et al. 2016, *ApJ*, 827, 118. <https://doi.org/10.3847/0004-637X/827/2/118>
- Lobanov, A. P. & Zensus, J. A. 2001, *Science*, 294, 128. <https://doi.org/10.1126/science.1063239>
- Longair, M. S. & Scheuer, P. A. G. 1967, *Nature*, 215, 919. <https://doi.org/10.1038/215919a0>
- Martini, P. 2004, in *Coevolution of Black Holes and Galaxies*, ed. L. C. Ho (Cambridge: Cambridge Univ. Press), 169
- Meyer, E. T., Sparks, W. B., Georganopoulos, M., et al. 2016, *ApJ*, 818, 195. <https://doi.org/10.3847/0004-637X/818/2/195>
- Netzer, H. 2013, *The Physics and Evolution of Active Galactic Nuclei* (Cambridge: Cambridge Univ. Press)
- Osterbrock, D. E. & Ferland, G. J. 2006, *Astrophysics of Gaseous Nebulae and Active Galactic Nuclei* (Sausalito, CA: Univ. Science Books)
- Pancoast, A., Brewer, B. J., & Treu, T. 2014a, *MNRAS*, 445, 3055. <https://doi.org/10.1093/mnras/stu1809>
- Pancoast, A., Brewer, B. J., Treu, T., et al. 2014b, *MNRAS*, 445, 3073. <https://doi.org/10.1093/mnras/stu1419>
- Papamakarios, G., Nalisnick, E., Rezende, D. J., Mohamed, S., Lakshminarayanan, B. 2021, *Journal of Machine Learning Research*, 22, 1
- Peterson, B. M. 1993, *PASP*, 105, 247. <https://doi.org/10.1086/133140>
- Peterson, B. M. 2014, *SSRv*, 183, 253. <https://doi.org/10.1007/s11214-013-9987-4>
- Peterson, B. M., Ferrarese, L., Gilbert, K. M., et al. 2004, *ApJ*, 613, 682. <https://doi.org/10.1086/423269>
- Peterson, B. M., Wanders, I., Bertram, R., et al. 1998, *ApJ*, 501, 82. <https://doi.org/10.1086/305813>
- Planck Collaboration, Aghanim, N., Akrami, Y., et al. 2020, *A&A*, 641, A6. <https://doi.org/10.1051/0004-6361/201833910>
- Rakshit, S., Petrov, R. G., Meilland, A., et al. 2015, *MNRAS*, 447, 2420. <https://doi.org/10.1093/mnras/stu2613>
- Richards, J. L., Max-Moerbeck, W., Pavlidou, V., et al. 2011, *ApJS*, 194, 29. <https://doi.org/10.1088/0067-0049/194/2/29>
- Risaliti, G. & Lusso, E. 2019, *Nature Astronomy*, 3, 272. <https://doi.org/10.1038/s41550-018-0657-z>
- Rees, M. J. 1977, *Eighth Texas Symposium on Relativistic Astrophysics*, 302, 613. <https://doi.org/10.1111/j.1749-6632.1977.tb37079.x>
- Rodríguez-Pascual, P. M., Alloin, D., Clavel, J., et al. 1997, *ApJS*, 110, 9. <https://doi.org/10.1086/312996>
- Roeser, H.-J. & Meisenheimer, K. 1991, *A&A*, 252, 458
- Savolainen, T., Wiik, K., Valtaoja, E., et al. 2006, *A&A*, 446, 71. <https://doi.org/10.1051/0004-6361:20053753>
- Salpeter, E. E. 1964, *ApJ*, 140, 796. <https://doi.org/10.1086/147973>
- Sandage, A. R. 1965, *AJ*, 70, 690. <https://doi.org/10.1086/109571>
- Schmidt, M. 1968, *ApJ*, 151, 393. <https://doi.org/10.1086/149446>
- Sivia, D., & Skilling, D. 2006, *Data Analysis: A Bayesian Tutorial* (New York: Oxford Univ. Press)
- Smith, P. S., Montiel, E., Rightley, S., et al. 2009, arXiv:0912.3621
- Smith, J. E., Young, S., Robinson, A., et al. 2002, *MNRAS*, 335, 773. <https://doi.org/10.1046/j.1365-8711.2002.05665.x>
- Songsheng, Y.-Y., Li, Y.-R., Du, P., et al. 2021, *ApJS*, 253, 57. <https://doi.org/10.3847/1538-4365/abe539>
- Songsheng, Y.-Y. & Wang, J.-M. 2018, *MNRAS*, 473, L1. <https://doi.org/10.1093/mnras/slx154>
- Songsheng, Y.-Y., Wang, J.-M., & Li, Y.-R. 2019, *ApJ*, 883, 184. <https://doi.org/10.3847/1538-4357/ab3c5e>
- Stern, J., Hennawi, J. F., & Pott, J.-U. 2015, *ApJ*, 804, 57. <https://doi.org/10.1088/0004-637X/804/1/57>
- Véron, P., Gonçalves, A. C., & Véron-Cetty, M.-P. 2002, *A&A*, 384, 826. <https://doi.org/10.1051/0004-6361:20020072>
- Wang, J.-M., Du, P., Brotherton, M. S., et al. 2017, *Nature Astronomy*, 1, 775. <https://doi.org/10.1038/s41550-017-0264-4>
- Wang, J.-M., Du, P., Valls-Gabaud, D., et al. 2013, *PhRvL*, 110, 081301. <https://doi.org/10.1103/PhysRevLett.110.081301>
- Wang, J.-M., Songsheng, Y.-Y., Li, Y.-R., et al. 2020, *Nature Astronomy*, 4, 517. <https://doi.org/10.1038/s41550-019-0979-5>
- Watson, D., Denney, K. D., Vestergaard, M., et al. 2011, *ApJL*, 740, L49. <https://doi.org/10.1088/2041-8205/740/2/L49>
- Williams, P. R., Pancoast, A., Treu, T., et al. 2018, *ApJ*, 866, 75. <https://doi.org/10.3847/1538-4357/aae086>
- Williams, P. R., Pancoast, A., Treu, T., et al. 2020, *ApJ*, 902, 74. <https://doi.org/10.3847/1538-4357/abbad7>

Williams, P. R., Treu, T., Dahle, H., et al. 2021, ApJL, 915, L9.

<https://doi.org/10.3847/2041-8213/ac081b>

Woltjer, L. 1959, ApJ, 130, 38. <https://doi.org/10.1086/146694>

Zhang, X., He, Z., Wang, T., et al. 2021, ApJ, 914, 143.

<https://doi.org/10.3847/1538-4357/abfb6b>

Zhang, Z.-X., Du, P., Smith, P. S., et al. 2019, ApJ, 876, 49.

<https://doi.org/10.3847/1538-4357/ab1099>